fluids

MDPI

Article

A Compact-Stencil Wetting Boundary Condition for Three-Dimensional Curved Surfaces in a Phase-Field Lattice Boltzmann Method

Makoto Sugimoto [1,*], Masayuki Kaneda [2], Kazuhiko Suga [2,3] and Masaya Shigeta [1]

[1] Department of Mechanical Systems Engineering, Tohoku University, 6-6-01 Aramaki Aza Aoba, Aoba-ku, Sendai 980-8579, Miyagi, Japan; shigeta@tohoku.ac.jp
[2] Department of Mechanical Engineering, Osaka Metropolitan University, 1-1 Gakuen-cho, Naka-ku, Sakai 599-8531, Osaka, Japan; mkaneda@omu.ac.jp (M.K.)
[3] Department of Mechanical Engineering, Otemon Gakuin University, 2-1-15 Nishiai, Ibaraki 567-8502, Osaka, Japan; k-suga@otemon.ac.jp (K.S.)
* Correspondence: msugimoto@tohoku.ac.jp

Abstract

Accurate numerical reproduction of contact line dynamics on three-dimensional curved solid surfaces remains a challenging issue in multiphase flow simulations. In this study, a wetting boundary condition applicable to curved surfaces is developed within a three-dimensional phase-field lattice Boltzmann framework. The proposed method extends an existing curved-surface wetting model and focuses on improving the evaluation of interface normals and order-parameter gradients on Cartesian lattices, while preserving the compact computational stencils and efficiency inherent to the lattice Boltzmann method. Three-dimensional simulations of liquid spreading on a concave spherical surface and droplet spreading on a convex solid sphere are performed over a wide range of prescribed contact angles. The results show that the proposed method eliminates nonphysical behaviors observed with conventional staircase-based boundary conditions, such as droplet sliding along the solid surface and droplet detachment into the surrounding gas phase. In the convex spherical surface cases, the droplet height converges stably to equilibrium through damped oscillations, and the equilibrium droplet shapes show good agreement with theoretical predictions derived from geometric considerations under zero-gravity conditions over a broad range of contact angles. These results demonstrate that the proposed wetting boundary condition can accurately reproduce wetting phenomena on three-dimensional curved solid surfaces.

Keywords: lattice Boltzmann method; phase-field model; liquid–gas two-phase flow; wettability; contact angle; boundary condition

Check for updates

Academic Editor: D. Andrew S. Rees

Received: 7 January 2026
Revised: 5 March 2026
Accepted: 12 March 2026
Published: 14 March 2026

Copyright: © 2026 by the authors. Licensee MDPI, Basel, Switzerland. This article is an open access article distributed under the terms and conditions of the Creative Commons Attribution (CC BY) license.

1. Introduction

Contact line dynamics governs the microscopic behavior in the region where a liquid–gas interface intersects a solid surface and plays a crucial role in a wide range of engineering and natural processes. For example, the control of wetting behavior critically influences the performance and efficiency of various applications such as enhanced oil recovery [1], carbon capture and storage [1,2], inkjet printing [3], spray cooling [4], and oil cooling devices [5]. In many of these practical systems, solid surfaces are not ideal flat planes but instead exhibit three-dimensional curvature or possess complex microstructures. Consequently, there

is a strong demand for accurate understanding and numerical reproduction of wetting phenomena and contact line dynamics on three-dimensional curved surfaces.

For fluid flows around such complex solid geometries, the lattice Boltzmann method (LBM) has emerged as an effective numerical approach. In the LBM, fluid motion is described in terms of distribution functions of virtual particles, and macroscopic flow dynamics are recovered through successive collision and streaming processes. At solid boundaries, the no-slip condition can be enforced by applying bounce-back schemes to the distribution functions, enabling efficient treatment of complex solid–fluid interfaces. Moreover, since the streaming process involves only local exchanges of distribution functions between neighboring lattice nodes, the LBM features compact computational stencils and high memory-access locality. These characteristics make the LBM highly suitable for large-scale parallel computations using the message passing interface (MPI) and graphics processing unit (GPU) architectures.

The lattice Boltzmann method has been further extended to multiphase flow simulations by coupling it with the phase-field model [6]. The phase-field model is a diffuse-interface approach in which surface tension is represented as a volumetric force acting within an interfacial region of finite thickness. This formulation enables large deformations of liquid–gas interfaces, as well as droplet and bubble coalescence and breakup, to be simulated with relative ease. In recent years, phase-field-based simulations have also been applied to evaporation processes of liquid phases [7–9], demonstrating their potential applicability to practical processes such as inkjet printing and phase-change cooling.

Within the framework of the phase-field lattice Boltzmann method (PFLBM), various wetting boundary conditions have been proposed to model wettability on solid surfaces, including approaches based on surface free-energy formulations [10,11] and those based on the geometric definition of the contact angle [11,12].

However, most existing wetting boundary conditions have been developed primarily for wetting phenomena on planar surfaces. In the LBM, uniformly spaced Cartesian lattices are typically employed, resulting in curved solid surfaces being approximated by staircase-like geometries. Under such approximations, accurate evaluation of the solid surface normal vector becomes difficult, which in turn degrades the fidelity of wetting simulations. Fakhari and Bolster [13] demonstrated that, when simulating a droplet in contact with a two-dimensional solid cylinder using a staircase-like approximation, the accuracy of wetting behavior reproduction deteriorates on both hydrophilic and hydrophobic surfaces. More generally, high-fidelity reproduction of wetting behavior requires accurate evaluation of the solid surface normal and an appropriate representation of its geometric relationship with the liquid–gas interface normal.

To address these limitations, wetting boundary conditions applicable to curved surfaces have been proposed in recent studies [13–15]. However, most of these developments have focused primarily on two-dimensional systems, and systematic validation of contact-angle reproducibility on three-dimensional curved surfaces remains limited.

The objective of this study is to establish a wetting boundary condition capable of accurately reproducing prescribed contact angles on three-dimensional curved solid surfaces within a phase-field lattice Boltzmann framework.

A representative approach for wetting boundary conditions on three-dimensional curved surfaces is the formulation proposed by Huang et al. [16,17]. In this method, a virtual order parameter is assigned to solid-phase lattice nodes near the contact line to reproduce the prescribed contact angle, under the assumption that the order parameter near the contact line follows an equilibrium interfacial profile. High accuracy has been demonstrated in two-dimensional, axisymmetric, and three-dimensional configurations. However, this formulation additionally assumes that the local curvature of the liquid–

gas interface is zero. Such an assumption may limit its theoretical consistency when a liquid–gas interface with substantial local curvature contact with a solid surface.

In contrast, the present study develops another approach in which the order parameter inside the solid phase is constructed by referencing the actual numerical distribution of the order parameter near the contact line. In this method, the influence of interface curvature is inherently embedded in the numerical distribution of the order parameter near the contact line, thereby eliminating the need to impose the zero local interface curvature assumption. Specifically, the wetting boundary condition originally proposed by Fakhari and Bolster [13] for two-dimensional curved surfaces is extended to three-dimensional configurations. Particular attention is paid to numerical inconsistencies arising from the evaluation of solid surface normals and order parameter gradients on three-dimensional curved geometries, while preserving the inherent high memory-access locality of the LBM. Using the proposed method, three-dimensional simulations of liquid spreading inside a spherical cavity and droplet spreading on a solid sphere are performed, and the accuracy of contact-angle reproduction on curved surfaces is quantitatively evaluated.

2. Methods

2.1. Governing Equations

In the phase-field model, the liquid and gas phases are distinguished by an order parameter ϕ, which represents the local volume fraction of the liquid phase. The values $\phi = 0$ and $\phi = 1$ correspond to the gas and liquid phases, respectively, while intermediate values $0 < \phi < 1$ define a diffuse interface with a finite thickness W. The time evolution of the order parameter ϕ is governed by the conservative Allen–Cahn equation [18,19],

$$\frac{\partial \phi}{\partial t} + \nabla \cdot (\phi \boldsymbol{u}) = \nabla \cdot \left\{ M_\phi \left[\nabla \phi - \frac{4\phi(1-\phi)}{W} \frac{\nabla \phi}{|\nabla \phi|} \right] \right\}, \tag{1}$$

where t denotes the time, $\boldsymbol{u}$ is the fluid velocity, and M_ϕ is the mobility coefficient. The conservation of the momentum is described by the Navier–Stokes equation,

$$\frac{\partial (\rho \boldsymbol{u})}{\partial t} + \nabla \cdot (\rho \boldsymbol{u}\boldsymbol{u}) = -\nabla p + \nabla \cdot \left\{ \mu \left[\nabla \boldsymbol{u} + (\nabla \boldsymbol{u})^{\mathrm{T}} \right] \right\} + \boldsymbol{F}_\sigma, \tag{2}$$

where ρ is the fluid density, p is the pressure, and μ is the dynamic viscosity. The superscript T denotes the transpose of a matrix. In the phase-field model, the surface tension force $\boldsymbol{F}_\sigma$ is incorporated as a volumetric force acting within the interfacial region. The surface tension force is evaluated using the following model [20,21]:

$$\boldsymbol{F}_\sigma = \mu_\phi \nabla \phi, \tag{3}$$

where μ_ϕ denotes the chemical potential, defined as

$$\mu_\phi = 4\beta\phi(\phi - 1)\left(\phi - \frac{1}{2}\right) - \kappa \nabla^2 \phi. \tag{4}$$

The coefficients β and κ are given by

$$\beta = \frac{12\sigma}{W}, \tag{5}$$

$$\kappa = \frac{3}{2}\sigma W, \tag{6}$$

where σ is the surface tension coefficient.

2.2. Phase-Field Lattice Boltzmann Method

In this study, the phase-field lattice Boltzmann method (PFLBM) proposed by Liang et al. [22] was employed to solve the conservative Allen–Cahn Equation (1) and the Navier–Stokes Equation (2). These governing equations are converted into the following lattice Boltzmann equations (LBEs):

$$f_i(\boldsymbol{x} + \boldsymbol{e}_i\delta_t,\ t + \delta_t) - f_i(\boldsymbol{x},\ t) = \Omega_i^f(\boldsymbol{x},\ t) + \delta_t R_i^f(\boldsymbol{x},\ t), \tag{7}$$

$$g_i(\boldsymbol{x} + \boldsymbol{e}_i\delta_t,\ t + \delta_t) - g_i(\boldsymbol{x},\ t) = \Omega_i^g(\boldsymbol{x},\ t) + \delta_t R_i^g(\boldsymbol{x},\ t), \tag{8}$$

where f_i and g_i denote the distribution functions for the order parameter ϕ and the fluid velocity $\boldsymbol{u}$, respectively. The terms Ω_i^f and Ω_i^g represent the collision operators, while R_i^f and R_i^g correspond to the source and forcing terms. The subscript i indicates the discrete velocity direction, $\boldsymbol{e}_i$ is the discrete velocity vector, and δ_t denotes the time step. In this study, the three-dimensional twenty-seven (D3Q27) discrete velocity model was adopted for both distribution functions.

In this study, the single-relaxation-time (SRT) model [23] was employed for the LBE for the order-parameter distribution function f_i. In contrast, the weighted multiple-relaxation-time (WMRT) model [24], which provides enhanced numerical stability, was employed for the LBE for the velocity distribution function g_i. The corresponding collision operators, Ω_i^f and Ω_i^g, are defined as

$$\boldsymbol{\Omega}^f = -\frac{1}{\tau_f}(\boldsymbol{f} - \boldsymbol{f}^{\mathrm{eq}}), \tag{9}$$

$$\boldsymbol{\Omega}^g = -\boldsymbol{M}^{-1}\boldsymbol{S}^g\boldsymbol{M}(\boldsymbol{g} - \boldsymbol{g}^{\mathrm{eq}}), \tag{10}$$

where the superscript "eq" denotes the local equilibrium distribution function, τ_f is the relaxation time for the order parameter, $\boldsymbol{M}$ is the transformation matrix used in the WMRT model, and $\boldsymbol{S}^g$ is the diagonal relaxation matrix in moment space. For the D3Q27 model, the set of discrete velocity vectors $\boldsymbol{e} = (\boldsymbol{e}_0,\ \boldsymbol{e}_1,\ \ldots,\ \boldsymbol{e}_{26})^{\mathrm{T}}$ is given by

$$\boldsymbol{e} = c\begin{bmatrix} 0 & 1 & -1 & 0 & 0 & 0 & 0 & 1 & -1 & 1 & -1 & 1 & -1 & 1 & -1 & 0 & 0 & 0 & 0 & 1 & -1 & -1 & 1 & 1 & -1 & 1 & -1 \\ 0 & 0 & 0 & 1 & -1 & 0 & 0 & 1 & -1 & -1 & 1 & 0 & 0 & 0 & 0 & 1 & -1 & 1 & -1 & 1 & -1 & 1 & -1 & -1 & 1 & 1 & -1 \\ 0 & 0 & 0 & 0 & 0 & 1 & -1 & 0 & 0 & 0 & 0 & 1 & -1 & -1 & 1 & 1 & -1 & -1 & 1 & 1 & -1 & 1 & -1 & 1 & -1 & -1 & 1 \end{bmatrix}^{\mathrm{T}}, \tag{11}$$

and the corresponding transformation matrix $\boldsymbol{M}$ is defined as [24]

$$
\boldsymbol{M} = \begin{bmatrix}
1 & 1 & 1 & 1 & 1 & 1 & 1 & 1 & 1 & 1 & 1 & 1 & 1 & 1 & 1 & 1 & 1 & 1 & 1 & 1 & 1 & 1 & 1 & 1 & 1 & 1 \\
0 & 1 & -1 & 0 & 0 & 0 & 0 & 1 & -1 & 1 & -1 & 1 & -1 & 1 & -1 & 0 & 0 & 0 & 0 & 1 & -1 & -1 & 1 & 1 & -1 & 1 & -1 \\
0 & 0 & 0 & 1 & -1 & 0 & 0 & 1 & -1 & -1 & 1 & 0 & 0 & 0 & 0 & 1 & -1 & 1 & -1 & 1 & -1 & 1 & -1 & -1 & 1 & 1 & -1 \\
0 & 0 & 0 & 0 & 0 & 1 & -1 & 0 & 0 & 0 & 0 & 1 & -1 & -1 & 1 & 1 & -1 & -1 & 1 & 1 & -1 & 1 & -1 & 1 & -1 & -1 & 1 \\
0 & 0 & 0 & 0 & 0 & 0 & 0 & 1 & 1 & -1 & -1 & 0 & 0 & 0 & 0 & 0 & 0 & 0 & 0 & 1 & 1 & -1 & -1 & -1 & -1 & 1 & 1 \\
0 & 0 & 0 & 0 & 0 & 0 & 0 & 0 & 0 & 0 & 0 & 0 & 0 & 0 & 0 & 1 & 1 & -1 & -1 & 1 & 1 & 1 & 1 & -1 & -1 & -1 & -1 \\
0 & 0 & 0 & 0 & 0 & 0 & 0 & 0 & 0 & 0 & 0 & 1 & 1 & -1 & -1 & 0 & 0 & 0 & 0 & 1 & 1 & -1 & -1 & 1 & 1 & -1 & -1 \\
0 & 2 & 2 & -1 & -1 & -1 & -1 & 1 & 1 & 1 & 1 & 1 & 1 & 1 & 1 & -2 & -2 & -2 & -2 & 0 & 0 & 0 & 0 & 0 & 0 & 0 & 0 \\
0 & 0 & 0 & 1 & 1 & -1 & -1 & 1 & 1 & 1 & 1 & -1 & -1 & -1 & -1 & 0 & 0 & 0 & 0 & 0 & 0 & 0 & 0 & 0 & 0 & 0 & 0 \\
-1 & 0 & 0 & 0 & 0 & 0 & 0 & 1 & 1 & 1 & 1 & 1 & 1 & 1 & 1 & 1 & 1 & 1 & 1 & 2 & 2 & 2 & 2 & 2 & 2 & 2 & 2 \\
0 & -2 & 2 & 0 & 0 & 0 & 0 & 1 & -1 & 1 & -1 & 1 & -1 & 1 & -1 & 0 & 0 & 0 & 0 & 4 & -4 & -4 & 4 & 4 & -4 & 4 & -4 \\
0 & 0 & 0 & -2 & 2 & 0 & 0 & 1 & -1 & -1 & 1 & 0 & 0 & 0 & 0 & 1 & -1 & 1 & -1 & 4 & -4 & 4 & -4 & -4 & 4 & 4 & -4 \\
0 & 0 & 0 & 0 & 0 & -2 & 2 & 0 & 0 & 0 & 0 & 1 & -1 & -1 & 1 & 1 & -1 & -1 & 1 & 4 & -4 & 4 & -4 & 4 & -4 & -4 & 4 \\
0 & 0 & 0 & 0 & 0 & 0 & 0 & 1 & -1 & 1 & -1 & -1 & 1 & -1 & 1 & 0 & 0 & 0 & 0 & 0 & 0 & 0 & 0 & 0 & 0 & 0 & 0 \\
0 & 0 & 0 & 0 & 0 & 0 & 0 & -1 & 1 & 1 & -1 & 0 & 0 & 0 & 0 & 1 & -1 & 1 & -1 & 0 & 0 & 0 & 0 & 0 & 0 & 0 & 0 \\
0 & 0 & 0 & 0 & 0 & 0 & 0 & 0 & 0 & 0 & 0 & 1 & -1 & -1 & 1 & -1 & 1 & 1 & -1 & 0 & 0 & 0 & 0 & 0 & 0 & 0 & 0 \\
0 & 0 & 0 & 0 & 0 & 0 & 0 & 0 & 0 & 0 & 0 & 0 & 0 & 0 & 0 & 0 & 0 & 0 & 0 & 1 & -1 & -1 & 1 & -1 & 1 & -1 & 1 \\
1 & -1 & -1 & -1 & -1 & -1 & -1 & 0 & 0 & 0 & 0 & 0 & 0 & 0 & 0 & 0 & 0 & 0 & 0 & 4 & 4 & 4 & 4 & 4 & 4 & 4 & 4 \\
0 & -2 & -2 & 1 & 1 & 1 & 1 & 2 & 2 & 2 & 2 & 2 & 2 & 2 & 2 & -4 & -4 & -4 & -4 & 0 & 0 & 0 & 0 & 0 & 0 & 0 & 0 \\
0 & 0 & 0 & -1 & -1 & 1 & 1 & 2 & 2 & 2 & 2 & -2 & -2 & -2 & -2 & 0 & 0 & 0 & 0 & 0 & 0 & 0 & 0 & 0 & 0 & 0 & 0 \\
0 & 0 & 0 & 0 & 0 & 0 & 0 & -1 & -1 & 1 & 1 & 0 & 0 & 0 & 0 & 0 & 0 & 0 & 0 & 2 & 2 & -2 & -2 & -2 & -2 & 2 & 2 \\
0 & 0 & 0 & 0 & 0 & 0 & 0 & 0 & 0 & 0 & 0 & 0 & 0 & 0 & 0 & -1 & -1 & 1 & 1 & 2 & 2 & 2 & 2 & -2 & -2 & -2 & -2 \\
0 & 0 & 0 & 0 & 0 & 0 & 0 & 0 & 0 & 0 & 0 & -1 & -1 & 1 & 1 & 0 & 0 & 0 & 0 & 2 & 2 & -2 & -2 & 2 & 2 & -2 & -2 \\
0 & 1 & -1 & 0 & 0 & 0 & 0 & -2 & 2 & -2 & 2 & -2 & 2 & -2 & 2 & 0 & 0 & 0 & 0 & 4 & -4 & -4 & 4 & 4 & -4 & 4 & -4 \\
0 & 0 & 0 & 1 & -1 & 0 & 0 & -2 & 2 & 2 & -2 & 0 & 0 & 0 & 0 & -2 & 2 & -2 & 2 & 4 & -4 & 4 & -4 & -4 & 4 & 4 & -4 \\
0 & 0 & 0 & 0 & 0 & 1 & -1 & 0 & 0 & 0 & 0 & -2 & 2 & 2 & -2 & -2 & 2 & 2 & -2 & 4 & -4 & 4 & -4 & 4 & -4 & -4 & 4 \\
-1 & 2 & 2 & 2 & 2 & 2 & 2 & -4 & -4 & -4 & -4 & -4 & -4 & -4 & -4 & -4 & -4 & -4 & -4 & 8 & 8 & 8 & 8 & 8 & 8 & 8 & 8
\end{bmatrix}, \tag{12}
$$

where $c = \delta_x/\delta_t$ is the lattice speed. The diagonal relaxation matrix $\boldsymbol{S}^g$ is given by [24]

$$
\boldsymbol{S}^g = \mathrm{diag}\big(1,1,1,1,s_g,s_g,s_g,s_g,s_g,1,1,1,1,1,1,1,1,1,1,1,1,1,1,1,1,1,1\big), \tag{13}
$$

with $s_g = 1/\tau_g$. The relaxation times τ_f and τ_g are related to the mobility coefficient M_ϕ and the kinematic viscosity ν, respectively, as

$$
M_\phi = c_\mathrm{s}^2\left(\tau_f - \frac{1}{2}\right)\delta_t, \tag{14}
$$

$$
\nu = c_\mathrm{s}^2\left(\tau_g - \frac{1}{2}\right)\delta_t, \tag{15}
$$

where $c_\mathrm{s} = c/\sqrt{3}$ is the speed of sound in the D3Q27 model.

The local equilibrium distribution function f_i^eq is constructed based on the first-order expansion of the Maxwell–Boltzmann distribution and is defined as

$$
f_i^\mathrm{eq} = w_i\phi\left(1 + \frac{\boldsymbol{e}_i \cdot \boldsymbol{u}}{c_\mathrm{s}^2}\right). \tag{16}
$$

The equilibrium distribution function for the velocity, g_i^{eq}, is described as [22,25]

$$g_i^{\mathrm{eq}} = \begin{cases} \frac{p}{c_s^2}(w_i - 1) + \rho s_i(\boldsymbol{u}), & i = 0, \\ \frac{p}{c_s^2} w_i + \rho s_i(\boldsymbol{u}), & i = 1, \ldots, 26, \end{cases} \tag{17}$$

where the function $s_i(\boldsymbol{u})$ is defined as

$$s_i(\boldsymbol{u}) = w_i \left[\frac{\boldsymbol{e}_i \cdot \boldsymbol{u}}{c_s^2} + \frac{(\boldsymbol{e}_i \cdot \boldsymbol{u})^2}{2c_s^4} - \frac{\boldsymbol{u} \cdot \boldsymbol{u}}{2c_s^2} \right]. \tag{18}$$

For the D3Q27 model, the weight coefficient w_i is expressed as

$$w_i = \frac{8}{27} \left(\frac{1}{4} \right)^{|e_{ix}| + |e_{iy}| + |e_{iz}|}. \tag{19}$$

To recover the macroscopic governing equations, the source term R_i^f and the forcing term R_i^g are introduced. These terms are defined as [22,24,26]

$$R_i^f = \left(1 - \frac{1}{2\tau_f} \right) w_i \boldsymbol{e}_i \cdot \left[\frac{\partial_t(\phi \boldsymbol{u})}{c_s^2} + \frac{4\phi(1-\phi)}{W} \frac{\nabla \phi}{|\nabla \phi|} \right], \tag{20}$$

$$\boldsymbol{R}^g = \boldsymbol{M}^{-1} \left(\boldsymbol{I} - \frac{\boldsymbol{S}^g}{2} \right) \boldsymbol{M} \overline{\boldsymbol{R}}^g, \tag{21}$$

where $\boldsymbol{I}$ denotes the identity matrix. The vector $\overline{\boldsymbol{R}}^g$ is given by

$$\overline{R}_i^g = w_i \left[\frac{\boldsymbol{e}_i \cdot \boldsymbol{F}_\sigma + (\boldsymbol{e}_i \cdot \boldsymbol{u})(\boldsymbol{e}_i \cdot \nabla \rho)}{c_s^2} \right]. \tag{22}$$

In this study, the time derivative in Equation (20) is evaluated using an explicit Euler scheme [22] as

$$\partial_t(\phi \boldsymbol{u}) = \frac{\phi(t)\boldsymbol{u}(t) - \phi(t - \delta_t)\boldsymbol{u}(t - \delta_t)}{\delta_t}. \tag{23}$$

The macroscopic variables—the order parameter ϕ, the fluid velocity $\boldsymbol{u}$, and the pressure p—are reconstructed from the zeroth- and first-order moments of the distribution functions as

$$\phi = \sum_i f_i, \tag{24}$$

$$\boldsymbol{u} = \frac{1}{\rho} \left(\sum_i \boldsymbol{e}_i g_i + \frac{\delta_t}{2} \boldsymbol{F}_\sigma \right), \tag{25}$$

$$p = \frac{c_s^2}{1 - w_0} \left[\sum_{i \neq 0} g_i + \rho s_0(\boldsymbol{u}) + \frac{\delta_t}{2} \boldsymbol{u} \cdot \nabla \rho \right]. \tag{26}$$

The fluid density ρ and kinematic viscosity ν are interpolated using the order parameter ϕ as

$$\rho = \phi \rho_l + (1 - \phi) \rho_g, \tag{27}$$

$$\nu = \phi \nu_l + (1 - \phi) \nu_g, \tag{28}$$

where the subscripts l and g denote the liquid and gas phases, respectively.

2.3. Boundary Conditions

2.3.1. Wetting Boundary Condition for the Order Parameter

Figure 1 illustrates a schematic diagram of a liquid–gas interface in contact with a solid wall at a contact angle θ. Here, $\boldsymbol{n}^{(\mathrm{sf})}$ denotes the unit normal vector of the solid surface pointing from the solid phase toward the fluid phase, while $\boldsymbol{n}^{(\mathrm{lg})}$ represents the unit normal vector of the liquid–gas interface pointing from the liquid phase toward the gas phase. At the contact line, the angle between the wall normal vector $\boldsymbol{n}^{(\mathrm{sf})}$ and the interface normal vector $\boldsymbol{n}^{(\mathrm{lg})}$ is equal to the contact angle θ. Therefore, the following geometric relation holds:

$$\left(\boldsymbol{n}^{(\mathrm{sf})} \cdot \boldsymbol{n}^{(\mathrm{lg})}\right)_{\mathrm{w}} = \cos\theta, \tag{29}$$

where the subscript w indicates the value at the wall surface. In Figure 1, ξ is defined as the signed distance from the liquid–gas interface, taking positive values in the gas phase and negative values in the liquid phase. Under this definition, the equilibrium solution of the one-dimensional conservative Allen–Cahn Equation (1) is given by [19]

$$\phi(\xi) = \frac{1}{2}\left(1 - \tanh\frac{2\xi}{W}\right). \tag{30}$$

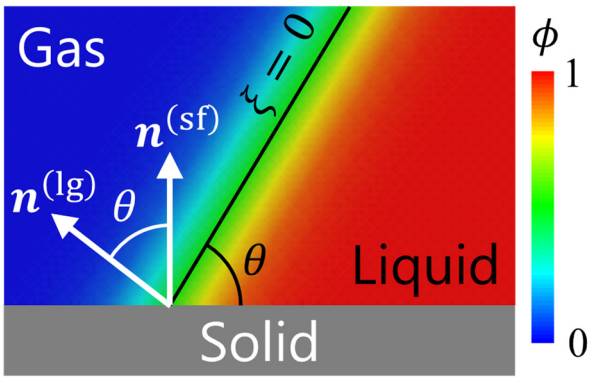


Figure 1. Schematic of a liquid–gas interface in contact with a solid surface at a contact angle θ.

From Equation (30), the gradient of the order parameter along the normal direction of the liquid–gas interface is expressed as

$$\frac{\partial\phi}{\partial\xi} = -\frac{4}{W}\phi(1-\phi). \tag{31}$$

Since the unit normal vector of the liquid–gas interface is defined as

$$\boldsymbol{n}^{(\mathrm{lg})} = -\frac{\nabla\phi}{|\nabla\phi|}, \tag{32}$$

Equation (29) yields the following relation at the wall:

$$\left(\boldsymbol{n}^{(\mathrm{sf})} \cdot \nabla\phi\right)_{\mathrm{w}} = -\frac{4}{W}\phi_{\mathrm{w}}(1-\phi_{\mathrm{w}})\cos\theta, \tag{33}$$

where ϕ_{w} denotes the order parameter at the wall surface. Furthermore, if a signed distance function ψ, which takes negative values inside the solid phase and positive values in the fluid phase, is known, the wall normal vector can be evaluated as

$$\boldsymbol{n}^{(\mathrm{sf})} = \nabla\psi. \tag{34}$$

By applying Equation (33) as a Neumann boundary condition for the order parameter, an arbitrary prescribed contact angle θ can be accurately imposed at the solid wall surface.

Fakhari and Bolster [13] employed Equation (33) to extrapolate the order parameter into the solid lattice nodes and evaluated the surface tension force using Equation (3) in the fluid nodes adjacent to the solid node. This procedure ensures that the prescribed contact angle θ is satisfied at fluid lattice nodes adjacent to the wall. In the following, the extrapolation procedure for the order parameter within the solid node is described in detail.

Figure 2 illustrates a representative example of the lattice-node arrangement around a curved solid surface. Although a two-dimensional curved surface is shown for clarity, the same extrapolation procedure is directly applicable to three-dimensional geometries. Let "s" denote a lattice node located inside the solid phase and adjacent to a fluid lattice node. The foot of the perpendicular dropped from node s onto the solid surface is denoted by "w". Furthermore, a fluid-phase point located on the same normal line is denoted by "f". The distances between s and w, and between w and f, are denoted by d_s and d_f, respectively. Assuming that the order parameter varies linearly between points s and f, the value of the order parameter at the wall and its normal gradient can be approximated from the order-parameter values at the fluid node ϕ_f and the solid node ϕ_s as

$$\phi_\mathrm{w} = \frac{d_\mathrm{s}\phi_\mathrm{f} + d_\mathrm{f}\phi_\mathrm{s}}{d_\mathrm{s} + d_\mathrm{f}}, \tag{35}$$

$$\left(\boldsymbol{n}^{(\mathrm{sf})} \cdot \nabla\phi\right)_\mathrm{w} = \frac{\phi_\mathrm{f} - \phi_\mathrm{s}}{d_\mathrm{s} + d_\mathrm{f}}. \tag{36}$$

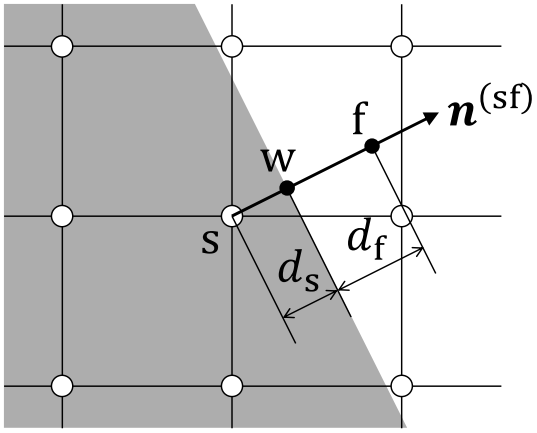


Figure 2. Schematic of lattice nodes near a curved solid surface illustrating the definition of points s, w, and f, and the distances d_s and d_f used in the extrapolation procedure.

By substituting Equations (35) and (36) into Equation (33) and solving the resulting quadratic equation for ϕ_s, the following expression is obtained:

$$\phi_\mathrm{s} = \frac{d_\mathrm{s} + d_\mathrm{f}}{2ad_\mathrm{f}}\left[1 + a - \sqrt{(1+a)^2 - 4a\phi_\mathrm{f}}\right] - \frac{d_\mathrm{s}}{d_\mathrm{f}}\phi_\mathrm{f}, \tag{37}$$

where

$$a = -\frac{4d_\mathrm{f}}{W}\cos\theta \neq 0, \quad \theta \neq 90^\circ. \tag{38}$$

For the special case of $\theta = 90^\circ$, the solution reduces to $\phi_\mathrm{s} = \phi_\mathrm{f}$. As described above, the wetting behavior can be reproduced by evaluating the surface tension force using the extrapolated order parameter obtained from Equation (37).

When evaluating Equation (37), the most intricate step is the computation of the order parameter ϕ_f at the fluid-phase point f. As illustrated in Figure 2, the wall normal

vector generally points in an arbitrary direction for curved surfaces, and thus ϕ_f must be obtained by interpolating the order parameter from surrounding lattice nodes. Fakhari and Bolster [13] proposed two interpolation strategies for this purpose. Figure 3 provides schematic illustrations of the two interpolation approaches.

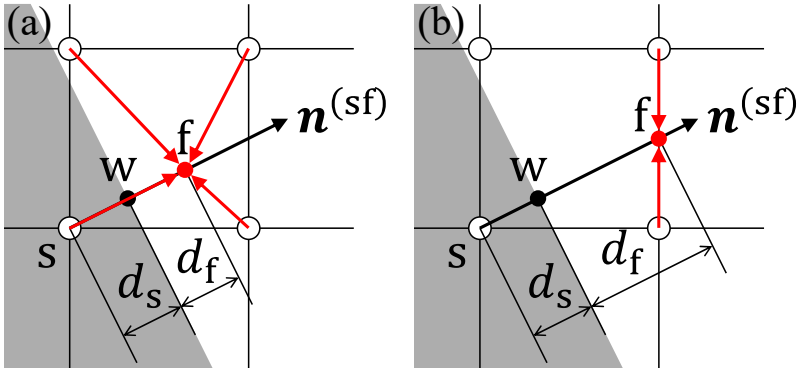


Figure 3. Schematic illustrations of the two interpolation approaches proposed by Fakhari and Bolster [13] for evaluating the order parameter at the fluid point f: (**a**) Interpolation using lattice nodes surrounding a point f placed such that $d_s = d_f$. (**b**) Interpolation using lattice nodes adjacent to the intersection point between the wall-normal line and a lattice grid. The red arrows indicate the reference relationships between the neighboring lattice nodes and the point f.

In the first approach, illustrated in Figure 3a, the point f is placed such that $d_s = d_f$, and the value of ϕ_f is interpolated using the lattice nodes surrounding this point. In this case, the reference lattice nodes may include the solid node s, which necessitates an iterative procedure to extrapolate ϕ_s. Moreover, when other solid-phase nodes are included among the reference lattice nodes, the interpolation procedure becomes more complicated. In addition, if d_s is large, the corresponding distance d_f also increases, which deteriorates the accuracy of the extrapolation for ϕ_s.

In the second interpolation approach, illustrated in Figure 3b, the point f is defined as the intersection between the wall-normal line and a lattice grid, and ϕ_f is interpolated from lattice nodes adjacent to this point. Although this approach eliminates the need for iterative calculations, the accuracy of the extrapolation for ϕ_s deteriorates as the distance d_f increases.

Fakhari and Bolster [13] employed these approaches to simulate liquid spreading on curved surfaces; however, their investigations were restricted to two-dimensional systems. Although the method is, in principle, extendable to three-dimensional configurations, the interpolation required to evaluate the order parameter ϕ_f becomes substantially more complex in three dimensions. This is because, on three-dimensional curved surfaces, the wall-normal vector may be oriented arbitrarily, and its intersection with a plane defined by lattice nodes cannot be uniquely determined. Consequently, a systematic procedure is required to select an appropriate interpolation plane for evaluating ϕ_f. Without such a procedure, the interpolation stencil may need to be enlarged, which can increase computational cost and potentially degrade extrapolation accuracy.

In the present study, a computational algorithm applicable to three-dimensional curved surfaces is developed based on the second interpolation approach. To preserve the accuracy of the extrapolation for ϕ_s, an additional strategy is introduced to keep the distance d_f sufficiently small while maintaining compact computational stencils.

In three-dimensional systems, interpolating the order parameter ϕ_f requires referencing at least three lattice nodes. Although numerous combinations of three lattice nodes are possible, in this study a combination satisfying all of the following constraints is selected:

Constraint 1. All referenced lattice nodes are located in the fluid phase.

Constraint 2. The separation between the referenced lattice nodes does not exceed δ_x along any coordinate direction.

Constraint 3. Among the combinations satisfying Constraints 1 and 2, the distance d_f is minimized.

Constraint 1 is imposed to avoid the iterative procedure described above. Constraint 2 is introduced to maintain both the accuracy of the interpolation and the locality of memory access. Constraint 3 is required to preserve high accuracy in the extrapolation of ϕ_s. In the following, a detailed procedure for searching combinations of lattice nodes that satisfy these three constraints is described. For simplicity, the case in which all components of the wall normal vector $\boldsymbol{n}^{(sf)}$ are positive is considered.

According to Constraint 2, the three referenced lattice nodes must be mutually adjacent on one of the following planes:

$$x = L_x\delta_x, \tag{39a}$$

$$y = L_y\delta_x, \tag{39b}$$

$$z = L_z\delta_x, \tag{39c}$$

$$x + y = L_{xy}\delta_x, \tag{39d}$$

$$y + z = L_{yz}\delta_x, \tag{39e}$$

$$z + x = L_{zx}\delta_x, \tag{39f}$$

$$x + y + z = L_{xyz}\delta_x, \tag{39g}$$

where the origin of the coordinate system is set at the lattice node s located inside the solid phase, and L_x, L_y, L_z, L_{xy}, L_{yz}, L_{zx}, and L_{xyz} are positive integers. When a component of the wall normal vector $\boldsymbol{n}^{(sf)}$ is negative, the sign of the corresponding coordinate in Equation (39) is reversed accordingly. Figure 4 illustrates the seven planes defined by Equation (39). For simplicity, $L = 1$ is assumed for all planes.

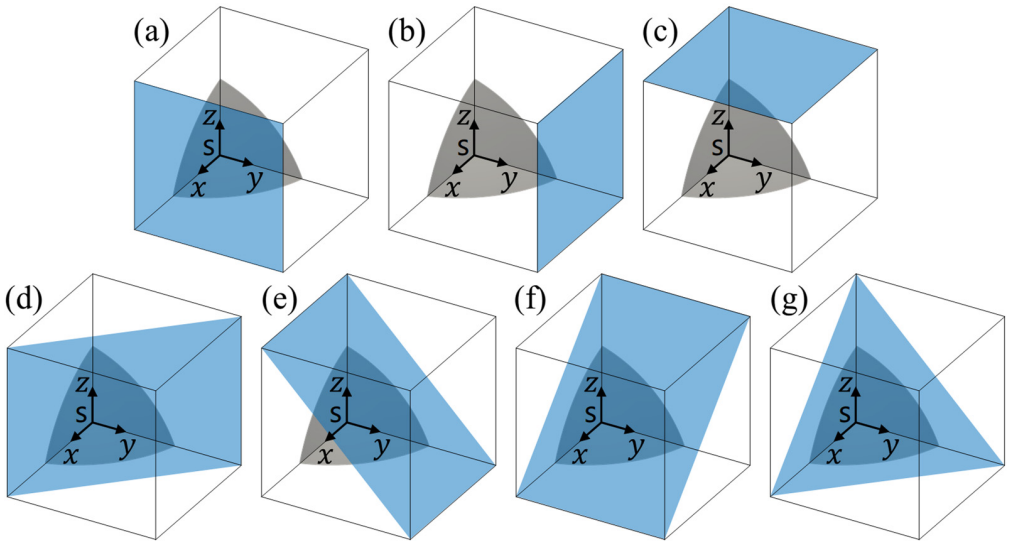


Figure 4. Seven planes considered for selecting lattice nodes used in the interpolation of the order parameter ϕ_f: **(a)** $x = \delta_x$; **(b)** $y = \delta_x$; **(c)** $z = \delta_x$; **(d)** $x + y = \delta_x$; **(e)** $y + z = \delta_x$; **(f)** $z + x = \delta_x$; **(g)** $x + y + z = \delta_x$.

The combination of lattice nodes used for interpolating the order parameter is determined according to the following procedure.

Step 0. Set $L_x = L_y = L_z = L_{xy} = L_{yz} = L_{zx} = L_{xyz} = 1$.

Step 1. Compute the coordinates of the intersection points between the wall-normal line extended from point s and the seven planes defined in Equation (39).

Step 2. Among the seven intersection points, select the one with the shortest distance from point s and denote it as f′.

Step 3. If the number of fluid-phase lattice nodes adjacent to point f′ on the corresponding plane defined by Equation (39) is less than three, increment the corresponding L value in Equation (39) by one and return to Step 1. If three such lattice nodes exist, proceed to Step 4. If four such lattice nodes exist, proceed to Step 5.

Step 4. If point f′ lies outside the triangle formed by the three lattice nodes, increment the corresponding L value in Equation (39) by one and return to Step 1. If point f′ lies inside the triangle, set f′ as f and evaluate the order parameter ϕ_f by linear interpolation using the values at the vertices of the triangle. Let the three lattice nodes be denoted by A, B, and C, with coordinates $\boldsymbol{x}_\mathrm{A} = (x_\mathrm{A},\ y_\mathrm{A},\ z_\mathrm{A})^\mathrm{T}$, $\boldsymbol{x}_\mathrm{B} = (x_\mathrm{B},\ y_\mathrm{B},\ z_\mathrm{B})^\mathrm{T}$, and $\boldsymbol{x}_\mathrm{C} = (x_\mathrm{C},\ y_\mathrm{C},\ z_\mathrm{C})^\mathrm{T}$, and corresponding order parameters ϕ_A, ϕ_B, and ϕ_C. The interpolation is expressed as

$$\phi_\mathrm{f} = \boldsymbol{\phi}^\mathrm{T}\boldsymbol{X}^{-1}\boldsymbol{x}_\mathrm{f}, \tag{40}$$

where $\boldsymbol{\phi} = (\phi_\mathrm{A},\ \phi_\mathrm{B},\ \phi_\mathrm{C})^\mathrm{T}$, $\boldsymbol{x}_\mathrm{f} = (x_\mathrm{f},\ y_\mathrm{f},\ z_\mathrm{f})^\mathrm{T}$, and $\boldsymbol{X} = (\boldsymbol{x}_\mathrm{A},\ \boldsymbol{x}_\mathrm{B},\ \boldsymbol{x}_\mathrm{C})$.

Step 5. First, set f′ as f. Among the four possible triangles formed by selecting three vertices from the four lattice nodes, identify the triangle that contains point f and minimizes the distance between its centroid g and point f. The order parameter at point f is then interpolated using Equation (40) with the vertices of the selected triangle. In the example shown in Figure 5, lattice nodes A, B, and D are used for the interpolation.

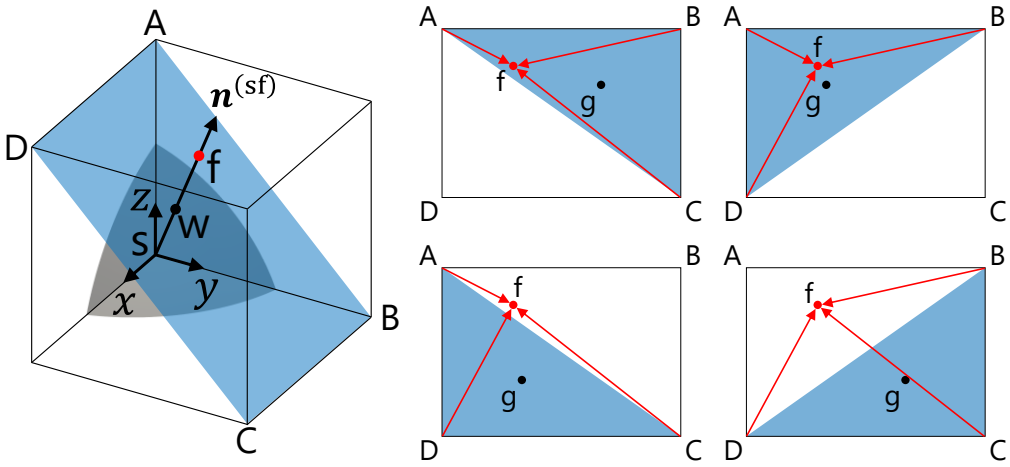


Figure 5. Schematic illustration of triangle selection for interpolating the order parameter ϕ_f when four candidate lattice nodes are present. The red arrows indicate the reference relationships between the neighboring lattice nodes and the point f.

2.3.2. Boundary Condition for the Distribution Functions

In the lattice Boltzmann method, the no-slip boundary condition at solid walls can be enforced by reflecting distribution functions that stream toward the wall and subsequently stream back to the original lattice node. This is referred to as the bounce-back scheme, for which several implementations have been proposed depending on the relative position between the wall surface and the lattice nodes. In this study, to accurately simulate flow fields around three-dimensional curved surfaces, an interpolated bounce-back scheme [27] is adopted for the velocity distribution function g_i, which allows the wall to be located at an arbitrary position relative to the lattice. In the interpolated bounce-back scheme, the

distribution function that streams back to a fluid lattice node F after being reflected at the wall is given by

$$g_{\bar{i}}(\boldsymbol{x}_{\mathrm{F}}, t+\delta_t) = \begin{cases} 2q g_i^*(\boldsymbol{x}_{\mathrm{F}}, t) + (1-2q) g_i^*(\boldsymbol{x}_{\mathrm{F}}, t+\delta_t), & 0 \le q < \frac{1}{2}, \\ \frac{1}{2q} g_i^*(\boldsymbol{x}_{\mathrm{F}}, t) + \left(1 - \frac{1}{2q}\right) g_{\bar{i}}^*(\boldsymbol{x}_{\mathrm{F}}, t), & \frac{1}{2} \le q < 1, \end{cases} \tag{41}$$

where g_i^* denotes the post-collision and pre-streaming distribution function, and $\boldsymbol{x}_{\mathrm{F}}$ is the position vector of fluid lattice node F. The subscript i indicates the discrete velocity direction pointing from node F toward the wall, and the opposite direction $\bar{i}$ satisfies $\boldsymbol{e}_{\bar{i}} = -\boldsymbol{e}_i$. The parameter q is related to the distance between the fluid lattice node F and the solid surface and is evaluated in this study as

$$q = \frac{|\boldsymbol{x}_{\mathrm{F}} - \boldsymbol{x}_{\mathrm{W}}|}{|\boldsymbol{x}_{\mathrm{F}} - \boldsymbol{x}_{\mathrm{S}}|} = \frac{\psi(\boldsymbol{x}_{\mathrm{F}})}{\psi(\boldsymbol{x}_{\mathrm{F}}) - \psi(\boldsymbol{x}_{\mathrm{S}})}, \tag{42}$$

where $\boldsymbol{x}_{\mathrm{W}}$ and $\boldsymbol{x}_{\mathrm{S}}$ denote the positions of the wall surface and the solid lattice node, respectively.

A bounce-back scheme must also be applied to the order-parameter distribution function f_i. However, it is known that the use of the interpolated bounce-back scheme may violate mass conservation for each phase [13,28]. Therefore, in this study, the following half-way bounce-back scheme is adopted for f_i:

$$f_{\bar{i}}(\boldsymbol{x}_{\mathrm{F}}, t+\delta_t) = f_i^*(\boldsymbol{x}_{\mathrm{F}}, t). \tag{43}$$

This formulation corresponds to Equation (41) with $q = 1/2$.

3. Results and Discussion

3.1. Validation Problems and Theoretical Predictions

3.1.1. Concave Spherical Surface

To validate the accuracy of the proposed wetting boundary condition, numerical simulations of liquid spreading on a concave spherical surface (i.e., a spherical cavity) were performed. Figure 6 illustrates the initial configuration. The lower half of a spherical cavity with radius R_{s} is filled with water, while the upper half is filled with air. The initial velocity of the entire system is zero, and the contact line moves according to the prescribed wall wettability after the simulation begins. In addition, the origin of the computational domain is defined at its center. At the initial state, the x- and y-axes are taken along the tangential directions of the liquid–gas interface, while the z-axis is defined in the normal direction. Under this coordinate system, the signed distance function ψ from the solid surface is expressed as

$$\psi = R_{\mathrm{s}} - |\boldsymbol{x}|. \tag{44}$$

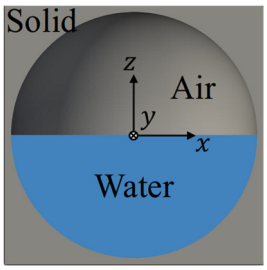


Figure 6. Initial configuration for liquid spreading in a spherical cavity. The lower hemisphere of the cavity (radius R_{s}) is filled with water, while the upper hemisphere is occupied by air.

By substituting this function into Equation (34), the wall normal vector $\boldsymbol{n}^{(\mathrm{sf})}$ can be obtained.

The wettability of the solid surface is prescribed by static contact angles in the range $30^\circ \leq \theta \leq 150^\circ$. The physical parameters are summarized in Table 1. To examine grid-resolution dependence, three different lattice resolutions were considered. The corresponding lattice spacing δ_x, time step δ_t, and lattice unit mass δ_m for each case are listed in Table 2. The mobility coefficient M_ϕ was fixed at $5.00 \times 10^{-2}\delta_x^2/\delta_t$, and the interfacial thickness W was maintained at $4\delta_x$ in all simulations.

Table 1. Physical properties and corresponding lattice-unit parameters used for the concave-surface validation cases. Three lattice resolutions (Cases 1–3) are considered to assess grid dependence.

Property/Parameter	SI Unit	Lattice Unit (Case 1)	Lattice Unit (Case 2)	Lattice Unit (Case 3)
Size of computational domain	1.07 mm × 1.07 mm × 1.07 mm	$80\delta_x \times 80\delta_x \times 80\delta_x$	$160\delta_x \times 160\delta_x \times 160\delta_x$	$240\delta_x \times 240\delta_x \times 240\delta_x$
Radius of solid surface R_s	0.5 mm	$37.5\delta_x$	$75.0\delta_x$	$112.5\delta_x$
Liquid density ρ_l	998.2 kg/m^3	$1.00\delta_m/\delta_x^3$	$1.00\delta_m/\delta_x^3$	$1.00\delta_m/\delta_x^3$
Gas density ρ_g	1.166 kg/m^3	$1.17 \times 10^{-3}\delta_m/\delta_x^3$	$1.17 \times 10^{-3}\delta_m/\delta_x^3$	$1.17 \times 10^{-3}\delta_m/\delta_x^3$
Kinematic viscosity of liquid ν_l	1.01×10^{-6} m^2/s	$5.68 \times 10^{-4}\delta_x^2/\delta_t$	$2.27 \times 10^{-3}\delta_x^2/\delta_t$	$5.11 \times 10^{-3}\delta_x^2/\delta_t$
Kinematic viscosity of gas ν_g	1.56×10^{-5} m^2/s	$8.78 \times 10^{-3}\delta_x^2/\delta_t$	$3.51 \times 10^{-2}\delta_x^2/\delta_t$	$7.90 \times 10^{-2}\delta_x^2/\delta_t$
Surface tension coefficient σ	72.88×10^{-3} N/m	$3.08 \times 10^{-4}\delta_m/\delta_t^2$	$2.46 \times 10^{-3}\delta_m/\delta_t^2$	$8.32 \times 10^{-3}\delta_m/\delta_t^2$

Table 2. Lattice spacing, time step, and lattice unit mass used in the concave-surface simulations.

Parameter	Case 1	Case 2	Case 3
Lattice spacing δ_x	13.3 μm	6.67 μm	4.44 μm
Time step δ_t	0.1 μs	0.1 μs	0.1 μs
Unit mass δ_m	2.37×10^{-12} kg	2.96×10^{-13} kg	8.76×10^{-14} kg

To assess the validity of the numerical results, the theoretical contact-line position is derived from geometric considerations. Figure 7 schematically illustrates the equilibrium configuration on hydrophilic and hydrophobic surfaces. Since gravity is neglected, the liquid–gas interface has constant curvature at equilibrium. O_1 and O_2 denote the centers of curvature of the solid surface and the liquid–gas interface, respectively. The radii of curvature are R_s and R_lg, and the contact-line radius is R_c. The angle between the line connecting O_1 and O_2 and the line connecting O_1 and the contact line is denoted by θ'. The liquid volume can be expressed as

$$\begin{aligned} V = {} & 2\pi\int_0^{\theta'}\int_0^{R_\mathrm{s}} r_1^2 \sin\theta_1 \mathrm{d}r_1\mathrm{d}\theta_1 + \tfrac{1}{3}\pi R_\mathrm{c}^2 R_\mathrm{s}\cos(\pi-\theta') \\ & -2\pi\int_0^{\theta'-\theta}\int_0^{R_\mathrm{lg}} r_2^2 \sin\theta_2 \mathrm{d}r_2\mathrm{d}\theta_2 + \tfrac{1}{3}\pi R_\mathrm{c}^2 R_\mathrm{lg}\cos(\theta'-\theta), \end{aligned} \tag{45}$$

where r_1 and r_2 denote distances from O_1 and O_2, respectively. Since the lower half of the cavity is initially filled with liquid, the initial volume is $V = 2\pi R_\mathrm{s}^3/3$. Substituting this into Equation (45) yields the following nonlinear equation for θ':

$$\frac{\left(-3\cos\theta' + \cos^3\theta'\right)\sin^3(\theta'-\theta)}{[2 - 3\cos(\theta'-\theta) + \cos^3(\theta'-\theta)]\sin^3\theta'} = 1. \tag{46}$$

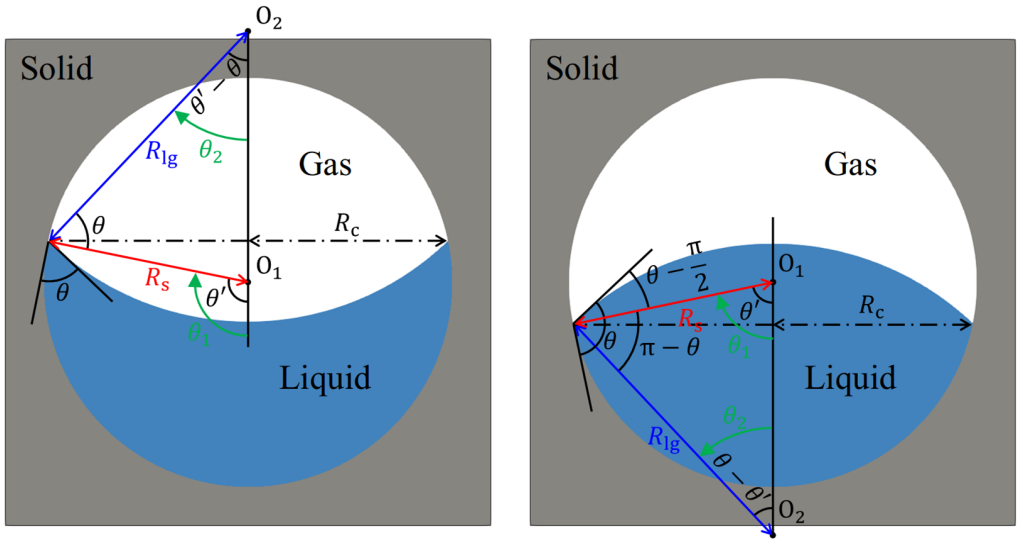


Figure 7. Geometric configurations used for the theoretical determination of the equilibrium contact-line position on a concave spherical surface. The centers of curvature of the solid surface and the liquid–gas interface are denoted by O_1 and O_2, respectively. R_s and R_{lg} represent the radii of curvature of the solid and liquid–gas interface, R_c is the contact-line radius, and θ' is the geometrically defined auxiliary angle corresponding to the prescribed contact angle θ. The left and right panels correspond to hydrophilic and hydrophobic conditions, respectively.

Note that $\theta' = 90^\circ$ in the case of $\theta = 90^\circ$. Equation (46) is solved numerically to obtain the theoretical value of θ', which serves as the reference for validation.

For reference, results obtained using a conventional staircase-based boundary treatment are also presented. Details of the conventional method are provided in Appendix A. Note that, even when the conventional method was used, the boundary conditions for the distribution functions were implemented using a combination of the half-way bounce-back scheme for f_i and the interpolated bounce-back scheme for g_i, as described in Section 2.3.2.

3.1.2. Convex Spherical Surface

Numerical simulations of a liquid droplet spreading on a convex solid sphere were also performed. Figure 8 shows the initial configuration. The origin of the computational domain is placed at its center. At the origin, a water droplet with an initial radius $R_{lg,0} = R_s$ is in contact with a solid sphere of radius R_s with zero initial velocity. The surrounding gas is air. When the x- and y-axes are defined along the tangential directions of the solid surface and the z-axis is taken in the normal direction, the signed distance function ψ from the solid surface is expressed as

$$\psi = |\boldsymbol{x} + R_s \boldsymbol{k}| - R_s, \tag{47}$$

where $\boldsymbol{k}$ is the unit vector in the z-direction. By substituting this function into Equation (34), the wall normal vector $\boldsymbol{n}^{(sf)}$ can be obtained. The physical properties are identical to those listed in Table 1. The size of computational domain is $200\delta_x \times 200\delta_x \times 200\delta_x$, corresponding to 2.67 mm × 2.67 mm × 2.67 mm.

In this case, simulations were conducted using the lattice units of Case 1 in Table 2. The wettability of the solid surface was prescribed in the same range $30^\circ \leq \theta \leq 150^\circ$, and the mobility coefficient M_ϕ and the interfacial thickness W were kept identical to those used in the concave case.

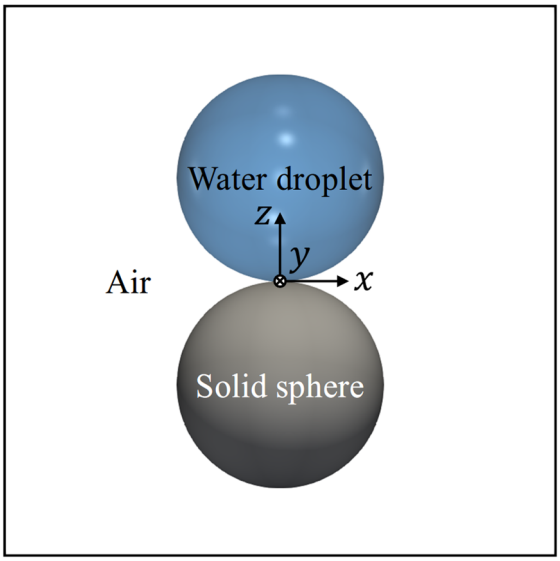


Figure 8. Initial configuration of a water droplet placed above a solid sphere in air.

As in the concave configuration, gravity is neglected; therefore, the equilibrium liquid–gas interface has uniform curvature. The theoretical equilibrium droplet geometry is determined from the prescribed contact angle and volume conservation. Figure 9 illustrates the geometric relations. The left panel corresponds to the case in which the position of the contact line is lower than the center of the solid sphere, whereas the right panel corresponds to the case in which it is higher. In these figures, H represents the distance from the solid surface to the droplet apex. The angle between the line connecting O_1 and O_2 and the line connecting O_1 and the contact line is denoted by θ'. Under these definitions, the nondimensional droplet height H/R_s is described as follows:

$$\frac{H}{R_s} = \cos\theta' - 1 + \frac{[1-\cos(\theta'+\theta)]\sin\theta'}{\sin(\theta'+\theta)}. \tag{48}$$

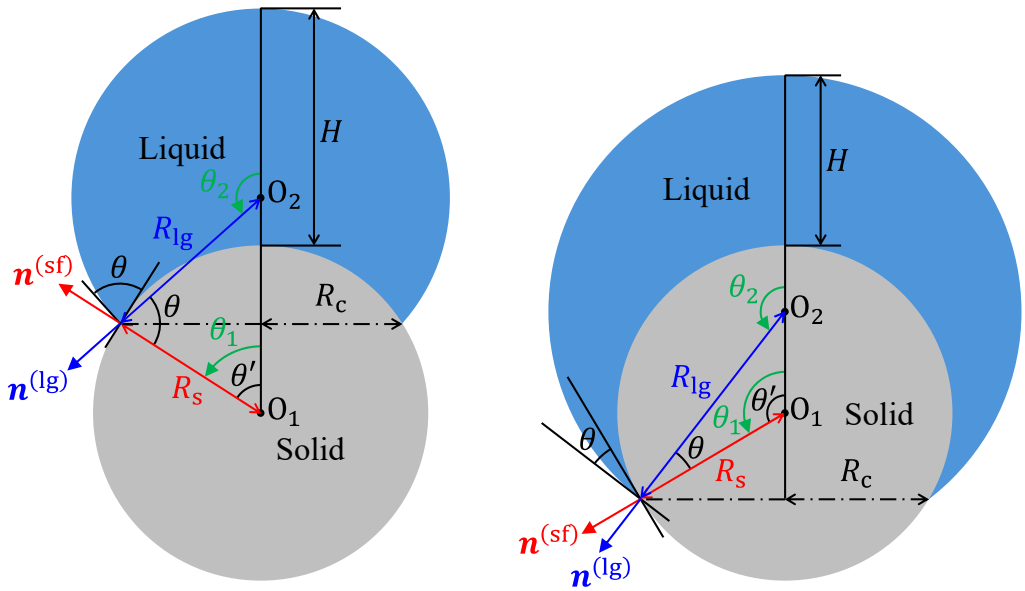


Figure 9. Schematic illustration of the equilibrium droplet geometries on a solid sphere used for the theoretical analysis.

The liquid volume can be expressed as

$$V = 2\pi\int_0^{\theta'+\theta}\int_0^{R_{lg}} r_2^2 \sin\theta_2 \mathrm{d}r_2\mathrm{d}\theta_2 + \tfrac{1}{3}\pi R_c^2 R_{lg}\cos[\pi-(\theta'+\theta)] \\ -2\pi\int_0^{\theta'}\int_0^{R_s} r_1^2 \sin\theta_1 \mathrm{d}r_1\mathrm{d}\theta_1 + \tfrac{1}{3}\pi R_c^2 R_s \cos\theta', \tag{49}$$

where r_1 and r_2 denote distances from O_1 and O_2, respectively. Substituting the initial volume $V = 4\pi R_{lg,0}^3/3 = 4\pi R_s^3/3$, Equation (49) yields the following nonlinear equation for θ':

$$\frac{(6-3\cos\theta'+\cos^3\theta')\sin^3(\theta'+\theta)}{[2-3\cos(\theta'+\theta)+\cos^3(\theta'+\theta)]\sin^3\theta'} = 1. \tag{50}$$

Equation (50) is solved numerically to determine θ', which is then substituted into Equation (48) to obtain the theoretical value of the droplet height H/R_s. In this study, the validity of the proposed method is assessed by comparing the nondimensional droplet height H/R_s obtained from the simulations with this theoretical prediction.

As in the concave case, results obtained using a conventional staircase-based boundary treatment are also presented for reference.

3.2. Liquid Spreading on a Concave Spherical Surface

Figure 10 presents snapshots of the liquid spreading on the concave spherical surface at $t = 10$ ms for the case with $\theta = 30^\circ$ using the parameter of Case 1. At this time, the interface has reached a steady state. Figure 10a,b correspond to the conventional and proposed methods, respectively. Figure 10(a-1,b-1) display the region $y \geq 0$. The planes labeled A–A and B–B indicate the cross-section at $z = 0.4R_s$, and the region $z \geq 0.4R_s$ is visualized in Figure 10(a-2,b-2).

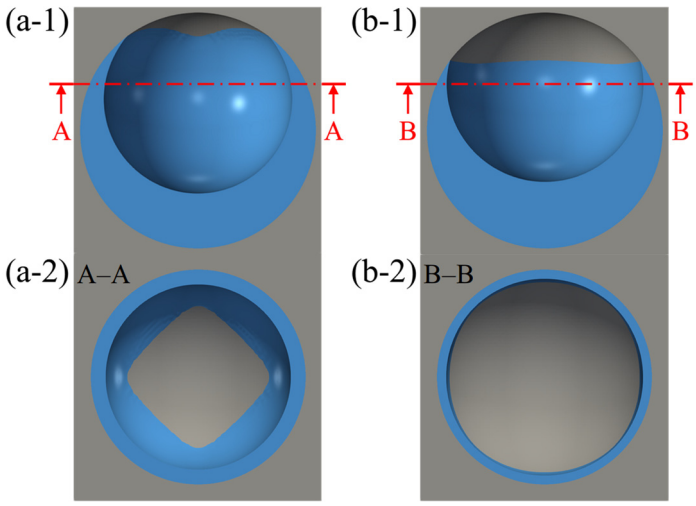


Figure 10. Liquid spreading on a concave spherical surface at $t = 10$ ms for $\theta = 30^\circ$ (Case 1 parameters): (**a**) simulated using the conventional method; (**b**) simulated using the proposed method. (**a-1**,**b-1**) show the region $y \geq 0$. (**a-2**,**b-2**) show cross-sectional views taken along planes A–A and B–B indicated by the red dashed lines in (**a-1**,**b-1**), respectively.

In the conventional method, the contact line exhibits a nearly polygonal shape, indicating nonphysical behavior due to the staircase approximation. In contrast, the proposed method produces an almost circular contact line, consistent with the expected axisymmetric equilibrium configuration.

To investigate grid-resolution dependence, simulations were conducted for Cases 1–3 under the condition $\theta = 30^\circ$. Figure 11 shows the interfaces, defined as the $\phi = 0.5$ contour, on the plane $y = 0$ at $t = 10$ ms, when it is stationary. In the figure, black, blue, and red

lines correspond to $R_s = 37.5\delta_x$ (Case 1), $75.0\delta_x$ (Case 2), and $112.5\delta_x$ (Case 3), respectively. Figure 11a shows results obtained using the conventional method, and Figure 11b shows those obtained using the proposed method. For both methods, the contact-line position shows negligible variation with grid resolution, indicating grid-independent behavior within the examined resolutions.

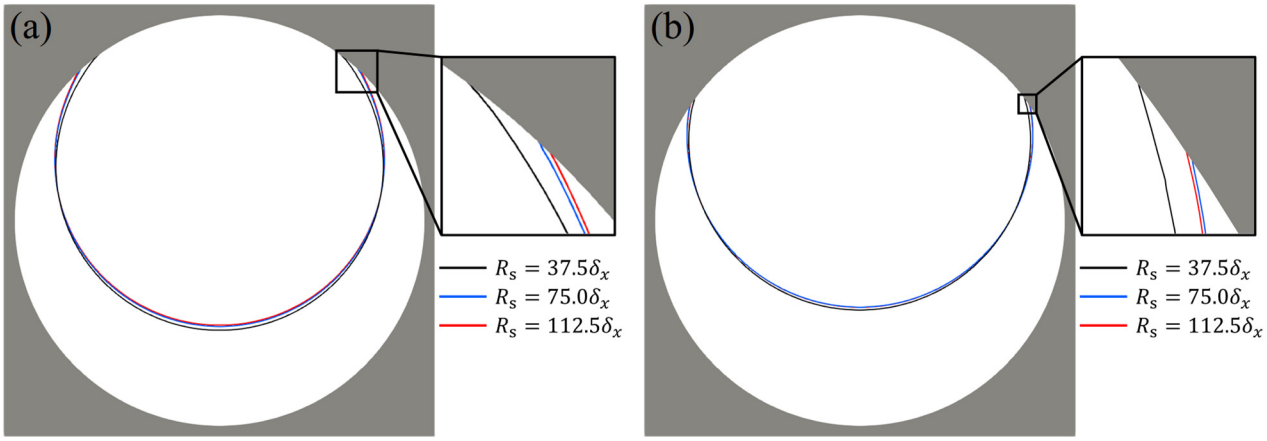


Figure 11. Cross-sectional profiles of the liquid–gas interface ($\phi = 0.5$) at $t = 10$ ms on the plane $y = 0$ for $\theta = 30°$: (**a**) simulated using the conventional method; (**b**) simulated using the proposed method. The inset panels show magnified views near the contact line. The black, blue, and red curves correspond to Case 1 ($R_s = 37.5\delta_x$), Case 2 ($75.0\delta_x$), and Case 3 ($112.5\delta_x$), respectively.

Figures 12 and 13 present the time evolution of the interface position obtained using the conventional and proposed methods, respectively. Panels a–e correspond to $\theta = 30°$, 60°, 90°, 120°, and 150°. Although the transient interface dynamics are qualitatively similar in both methods, noticeable differences are observed in the final contact-line positions at $t = 10$ ms. For the hydrophilic surface, the contact line predicted by the conventional method (Figure 12a) appears at a higher location compared with that predicted by the proposed method (Figure 13a), whereas the opposite trend is observed for the hydrophobic surface (Figures 12e and 13e). These differences suggest that the two boundary treatments yield distinct equilibrium configurations under identical prescribed contact angles.

Figure 14 quantitatively compares the computed values of θ' with the corresponding theoretical predictions. The black solid line represents the theoretical solution obtained from Equation (46), while the blue and red symbols denote the results obtained using the conventional and proposed methods, respectively. For the conventional method, systematic deviations from the theoretical prediction are observed across the examined contact-angle range. In particular, the angle θ' is overestimated on hydrophilic surfaces and underestimated on hydrophobic surfaces. When these deviations are converted into the corresponding error in the contact angle θ, the conventional method yields errors ranging from 11.3° to 25.9° for $\theta < 60°$ and $\theta > 120°$.

In contrast, the proposed method shows substantially improved agreement with the theoretical prediction. Although small deviations remain at extreme wettabilities ($\theta = 30°$ and 150°), the corresponding errors in the contact angle θ are limited to 8.2° and 8.3°, respectively. Furthermore, for $45° \leq \theta \leq 135°$, the error is reduced to less than 5° over the entire range. These results demonstrate that the proposed method effectively enhances contact-angle reproducibility on concave curved surfaces.

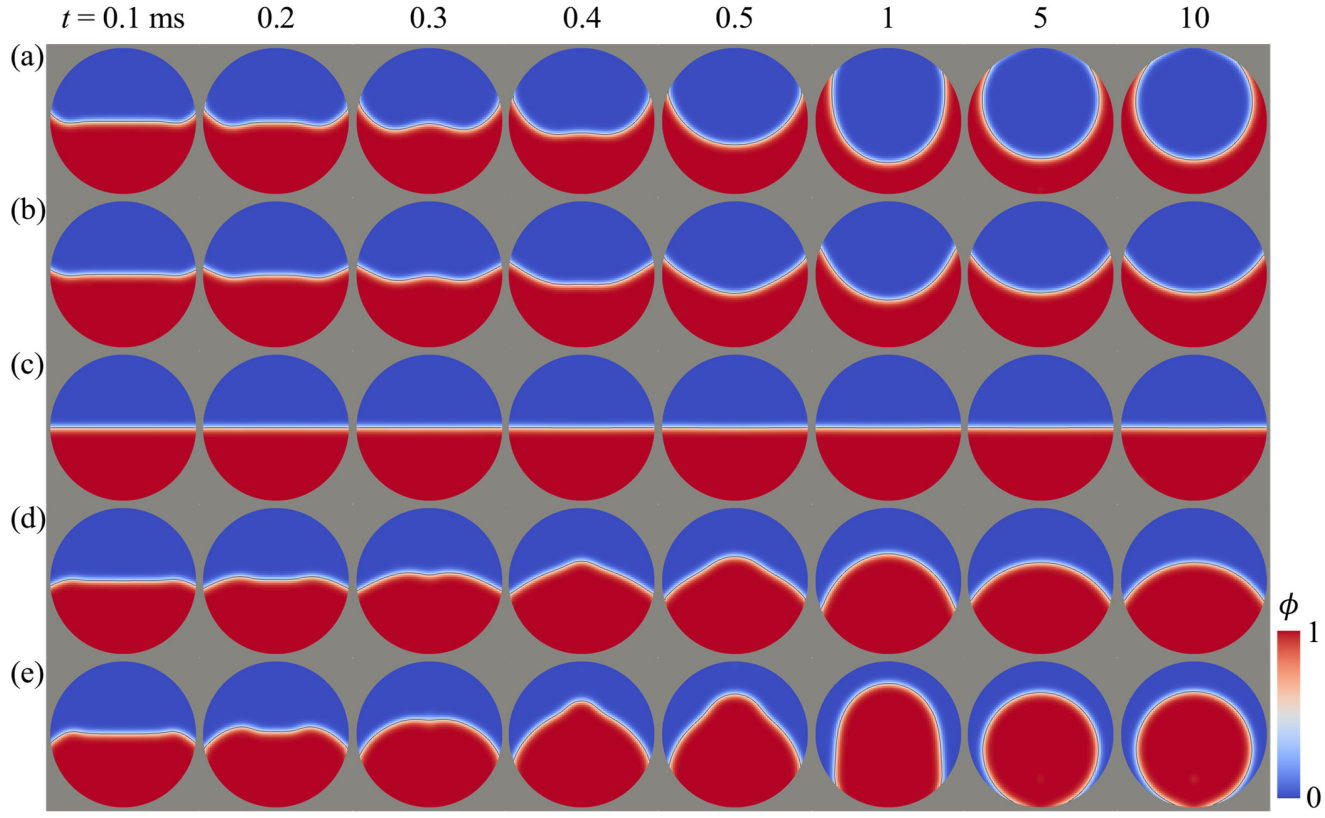


Figure 12. Snapshots of liquid spreading on the concave spherical surfaces simulated using the conventional wetting boundary condition: (**a**) $\theta = 30°$; (**b**) $\theta = 60°$; (**c**) $\theta = 90°$; (**d**) $\theta = 120°$; (**e**) $\theta = 150°$.

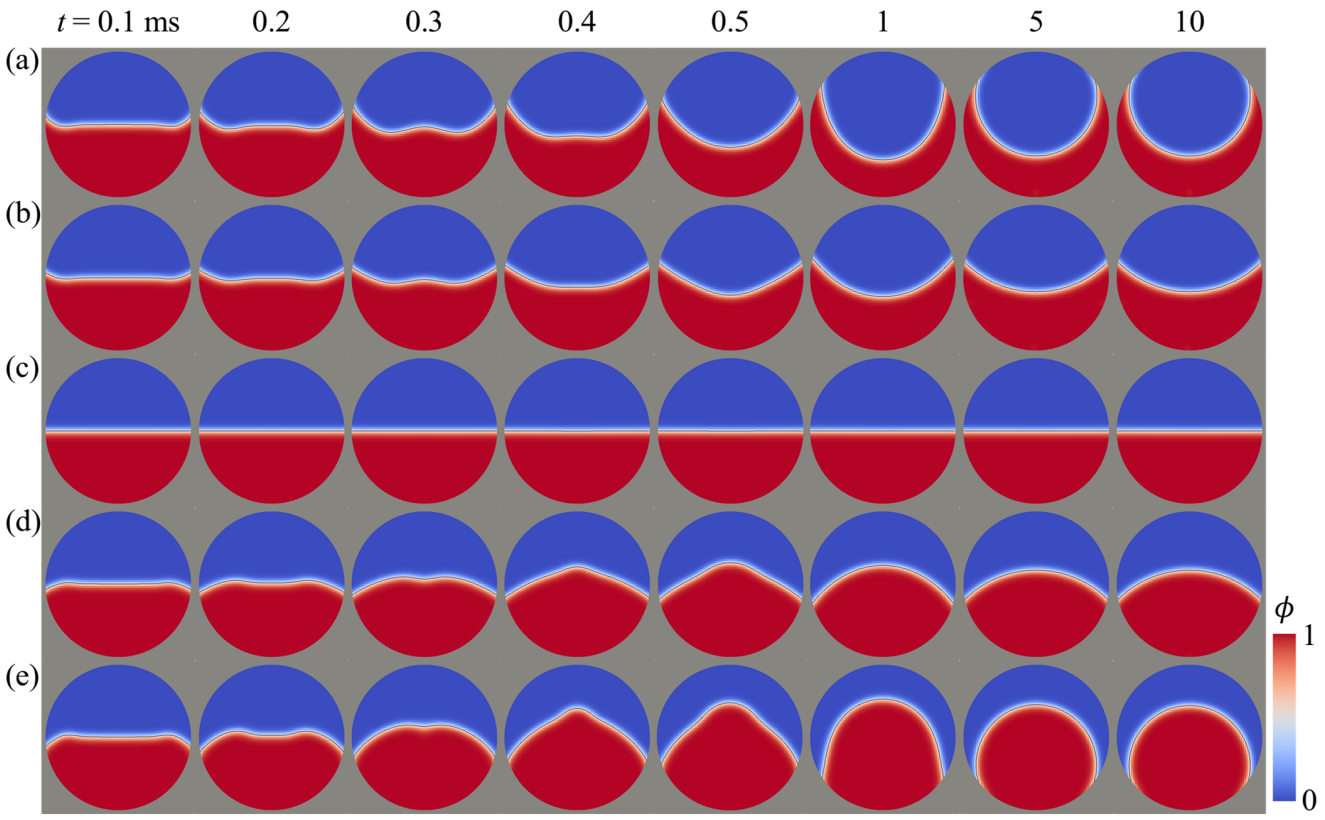


Figure 13. Snapshots of liquid spreading on the concave spherical surfaces simulated using the proposed wetting boundary condition: (**a**) $\theta = 30°$; (**b**) $\theta = 60°$; (**c**) $\theta = 90°$; (**d**) $\theta = 120°$; (**e**) $\theta = 150°$.

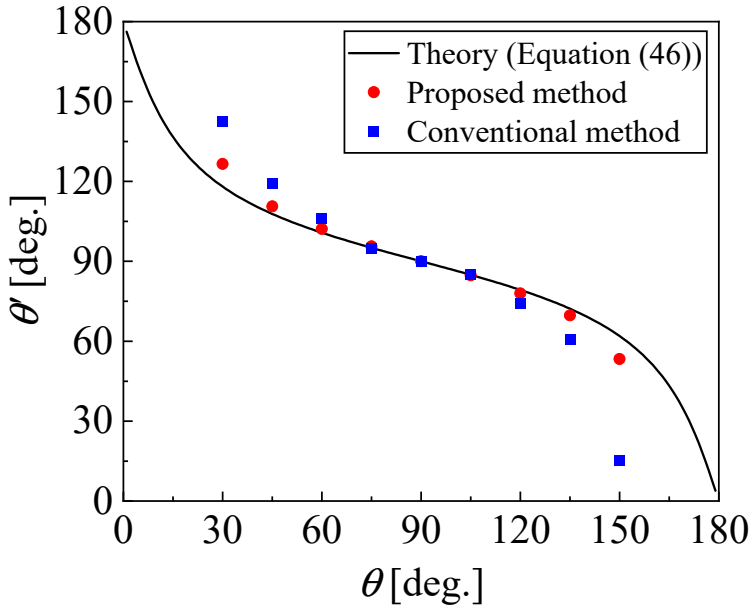


Figure 14. Comparison of the predicted θ' as a function of the prescribed contact angle θ for the concave spherical surface.

3.3. Droplet Spreading on a Convex Spherical Surface

Figure 15 represents snapshots of a liquid droplet spreading on a solid sphere computed using the conventional method, where the liquid–gas interface is visualized by the isosurface of the order parameter $\phi = 0.5$. Figure 15a–e correspond to prescribed contact angles $\theta = 30^\circ$, 60°, 90°, 120°, and 150°, respectively. For $\theta = 60^\circ$ and 120°, the conventional method qualitatively reproduces reasonable wetting behavior (Figure 15b,d). However, for $\theta = 90^\circ$, the droplet exhibits nonphysical sliding motion along the sphere surface (Figure 15c). Furthermore, for $\theta = 150^\circ$, the droplet does not wet the solid surface and instead detaches and disperses into the surrounding air (Figure 15e), which is clearly unphysical.

To clarify the origin of these behaviors, Figure 16 presents an example of the contact line on a curved solid surface. Points $s_1, \ldots, s_5$ denote solid-phase lattice nodes adjacent to the fluid phase. In the conventional method, the curved solid surface is approximated by a staircase geometry (black dashed line). The black arrows represent the wall-normal vectors evaluated under this approximation, while the red arrows correspond to those obtained by the proposed method. The fluid-phase reference points used in the extrapolation procedure (Equation (37)) are denoted by $f_1, \ldots, f_5$. The color of the fluid phase represents the order parameter, which decreases from left to right in the figure.

Because the staircase approximation limits the accuracy of the wall-normal evaluation, the extrapolated order parameter is overestimated at nodes s_1 and s_2, and underestimated at s_3, s_4, and s_5. Consequently, the order-parameter gradient near the contact line becomes excessively large because it is computed using neighboring solid nodes whose extrapolated values are inconsistently over- and underestimated (e.g., at s_2 and s_3). This leads to an artificially amplified surface tension force. This artificial amplification of the surface tension force destabilizes the contact line and leads to the nonphysical motion observed in Figure 15.

Figure 17 shows the corresponding results obtained using the proposed method. For all prescribed contact angles, no nonphysical sliding or droplet detachment is observed. Notably, for $\theta = 30^\circ$, the conventional method predicts complete engulfment of the solid sphere by the droplet (Figure 15a), whereas the proposed method yields a stable contact line located approximately halfway around the sphere (Figure 17a), which is consistent with geometric expectations.

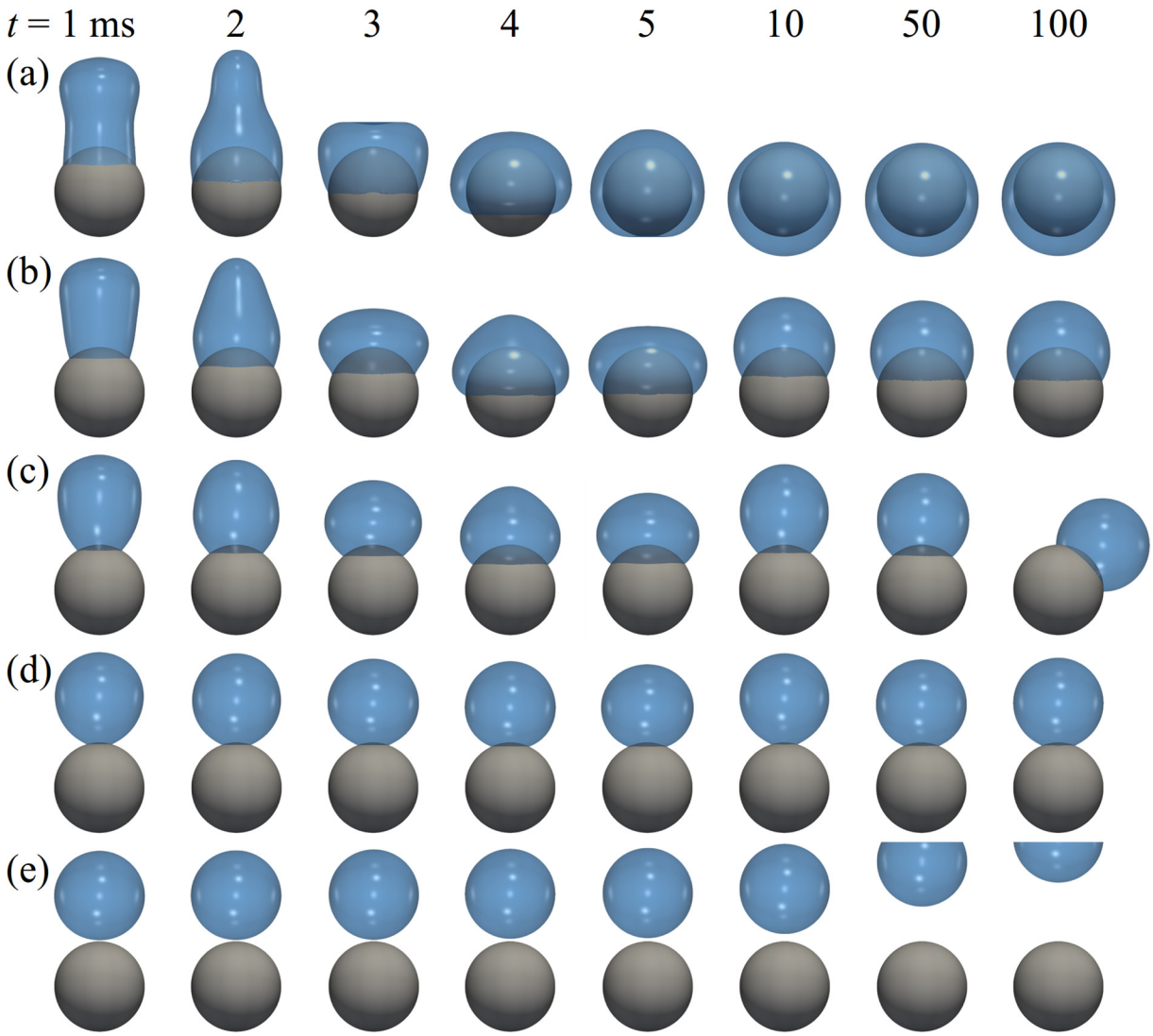


Figure 15. Snapshots of liquid droplets spreading on the solid spheres simulated using the conventional wetting boundary condition: (**a**) $\theta = 30°$; (**b**) $\theta = 60°$; (**c**) $\theta = 90°$; (**d**) $\theta = 120°$; (**e**) $\theta = 150°$.

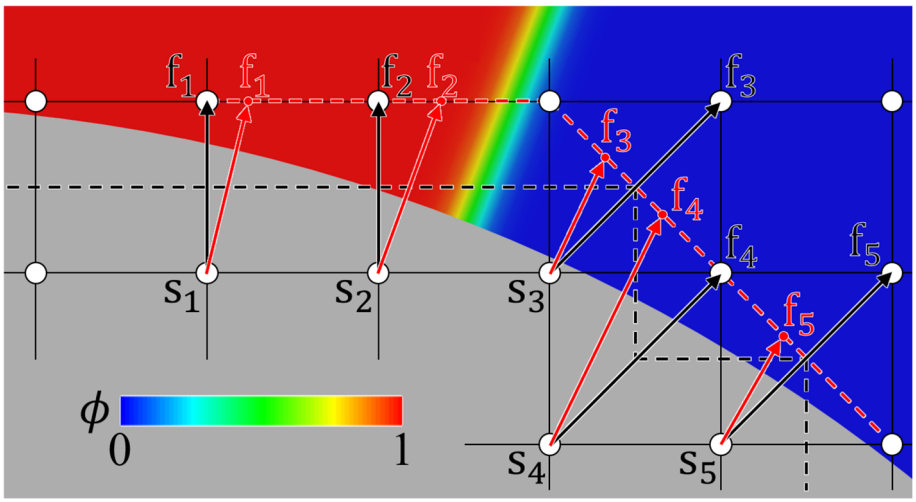


Figure 16. Schematic comparison of the extrapolation procedure for the order parameter near a curved solid boundary in the conventional and proposed methods. The black dashed line represents the solid surface in the conventional method, while the red dashed line indicates the plane used for interpolating the order parameter in the proposed method.

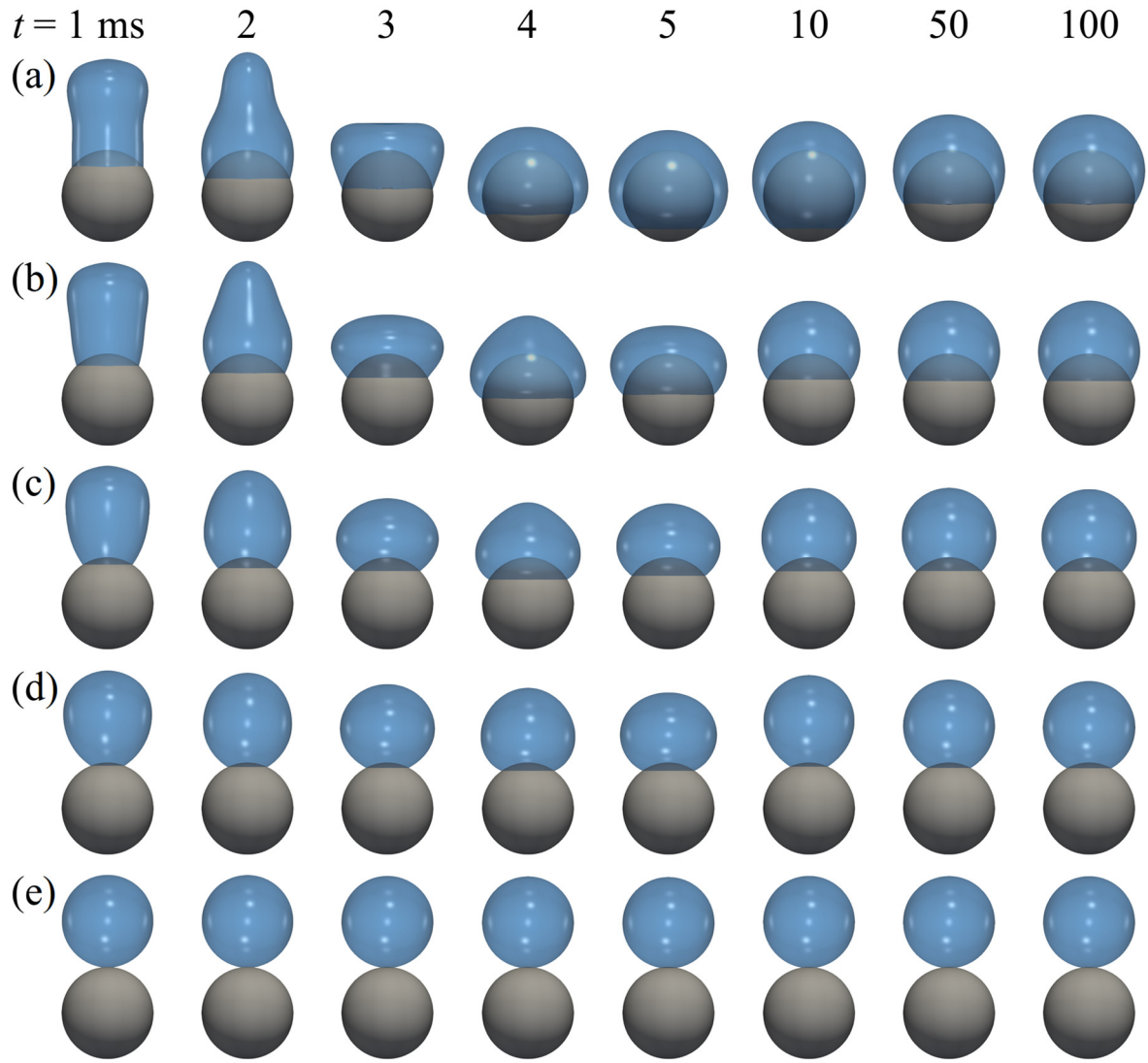


Figure 17. Snapshots of liquid droplets spreading on the solid spheres simulated using the proposed wetting boundary condition: (**a**) $\theta = 30°$; (**b**) $\theta = 60°$; (**c**) $\theta = 90°$; (**d**) $\theta = 120°$; (**e**) $\theta = 150°$.

Figure 18 presents the time evolution of the nondimensional droplet height H/R_s. In the conventional method (Figure 18a), the nondimensional droplet height H/R_s cannot be evaluated accurately for $\theta = 75°$, 90°, and 105° due to the nonphysical sliding of the droplet along the solid surface, as observed in Figure 15c. In addition, the increase in H/R_s observed for $\theta = 150°$ is attributed to the detachment and dispersion of the droplet from the solid surface, as shown in Figure 15e. In contrast, the proposed method (Figure 18b) shows convergence of H/R_s to constant values through damped oscillations for all contact angles.

Figure 19 compares the steady nondimensional droplet height H/R_s with the theoretical prediction. The solid line represents the ideal nondimensional droplet height obtained by numerically solving Equation (50) for θ' and substituting the solution into Equation (48). The blue square symbols indicate the results obtained using the conventional method, while the red circular symbols denote those obtained using the proposed method. For the conventional method, cases without steady solutions ($\theta = 75°$, 90°, 105°, and 150°) and the case in which the solid sphere is completely engulfed by the droplet ($\theta = 30°$) are excluded. Although slight deviations are observed at extreme contact angles ($\theta = 30°$ and 150°), the proposed method accurately reproduces the theoretical wetting behavior over a wide range of contact angles, $45° \leq \theta \leq 135°$. When these deviations are converted into

the corresponding error in the contact angle θ, the proposed method yields an error of 11.0° at $\theta = 150°$, whereas the error remains within 5° for $30° \leq \theta \leq 135°$.

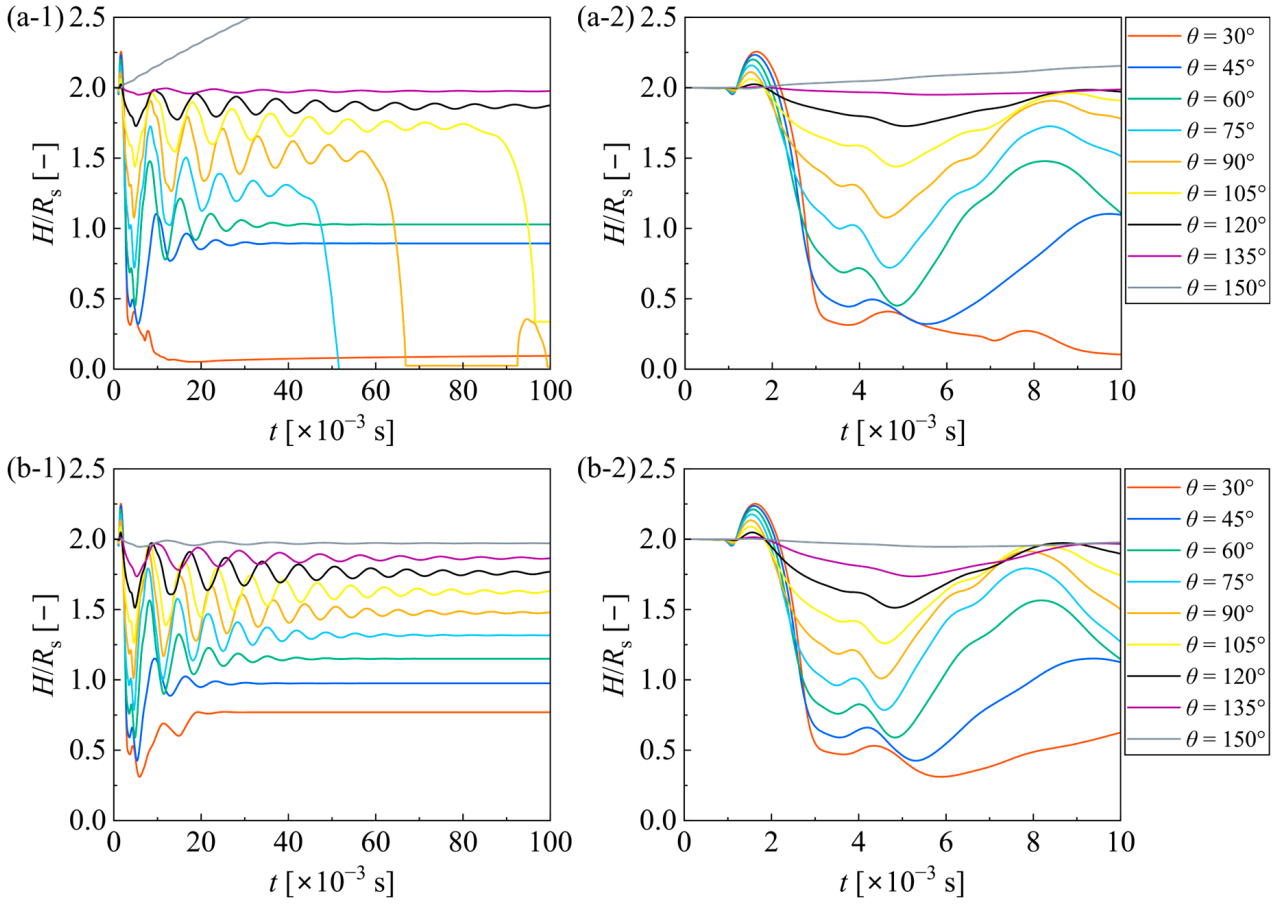


Figure 18. Time evolution of the nondimensional droplet height H/R_s for different contact angles θ: (**a**) simulated using the conventional method; (**b**) simulated using the proposed method. (**a-1**,**b-1**) show the results for $t \leq 100$ ms. (**a-2**,**b-2**) show the results for $t \leq 10$ ms.

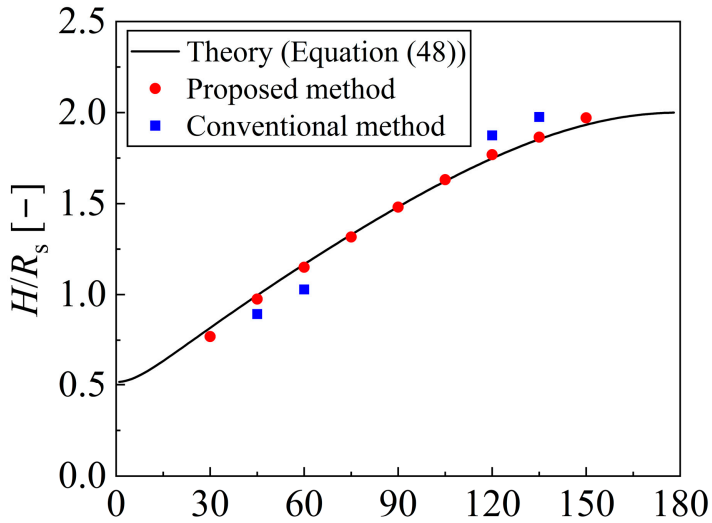


Figure 19. Equilibrium values of the nondimensional droplet height H/R_s extracted from the time evolution shown in Figure 18, compared with the theoretical prediction.

4. Conclusions

In this study, a wetting boundary condition capable of accurately reproducing prescribed contact angles on three-dimensional curved solid surfaces was developed within a phase-field lattice Boltzmann framework. The proposed method extends an existing curved-surface wetting model to three-dimensional geometries while preserving the compact computational stencils inherent to the lattice Boltzmann method.

Three-dimensional simulations of liquid spreading on a concave spherical surface and droplet spreading on a convex solid sphere demonstrated that the proposed method eliminates nonphysical behaviors observed with conventional staircase-based approaches, such as droplet sliding and detachment. The equilibrium droplet shapes showed good agreement with theoretical predictions over a wide range of contact angles, confirming the accuracy of the proposed wetting boundary condition on curved surfaces.

Owing to its computational locality and compatibility with parallel computing architectures, the method is well suited for large-scale simulations involving realistic solid geometries. Future work will focus on extending the present framework to multiphysics problems, such as phase change and heat transfer.

Author Contributions: Conceptualization, M.S. (Makoto Sugimoto); methodology, M.S. (Makoto Sugimoto), M.K. and K.S.; software, M.S. (Makoto Sugimoto); validation, M.S. (Makoto Sugimoto); formal analysis, M.S. (Makoto Sugimoto); investigation, M.S. (Makoto Sugimoto); resources, M.S. (Makoto Sugimoto) and M.S. (Masaya Shigeta); data curation, M.S. (Makoto Sugimoto); writing—original draft preparation, M.S. (Makoto Sugimoto); writing—review and editing, M.K., K.S. and M.S. (Masaya Shigeta); visualization, M.S. (Makoto Sugimoto); supervision, M.K., K.S. and M.S. (Masaya Shigeta); project administration, M.S. (Makoto Sugimoto); funding acquisition, M.S. (Makoto Sugimoto). All authors have read and agreed to the published version of the manuscript.

Funding: This research was funded by Japan Society for the Promotion of Science KAKENHI grant number 25K17537.

Data Availability Statement: Data will be made available on request.

Conflicts of Interest: The authors declare no conflicts of interest.

Nomenclature

a	Function used in the extrapolation of the order parameter	[–]
c	Lattice speed	[m/s]
c_s	Speed of sound	[m/s]
d_f	Distance between points f and w	[m]
d_s	Distance between points s and w	[m]
$\boldsymbol{e}_i$	Discrete velocity vector	[m/s]
f_i	Distribution function for the order parameter	[–]
$\boldsymbol{F}_\sigma$	Volumetric surface tension force	[N/m^3]
g_i	Distribution function for the fluid velocity	[kg/m^3]
H	Distance from the solid surface to the droplet apex	[m]
$\boldsymbol{I}$	Identity matrix	[–]
$\boldsymbol{k}$	Unit vector in the z-direction	[–]
L_x, L_y, L_z, L_{xy}, L_{yz}, L_{zx}, L_{xyz}	Positive integers	[–]
$\boldsymbol{M}$	Transformation matrix used in the WMRT model	
M_ϕ	Mobility coefficient	[m^2/s]
$\boldsymbol{n}^{(\mathrm{lg})}$	Unit normal vector of the liquid–gas interface pointing from the liquid phase toward the gas phase	[–]

$\boldsymbol{n}^{(\mathrm{sf})}$	Unit normal vector of the solid surface pointing from the solid phase toward the fluid phase	[–]
p	Pressure	[Pa]
q	Parameter related to the distance between the fluid lattice node and the solid surface	[–]
r_1	Distance from O_1	[m]
r_2	Distance from O_2	[m]
R_c	Radius of contact line	[m]
R_i^f	Source term	[1/s]
R_i^g, $\overline{R}_i^g$	Forcing terms	[kg/(m^3 s)]
R_lg	Radius of droplet	[m]
$R_{\mathrm{lg},\,0}$	Initial radius of droplet	[m]
R_s	Radius of solid surface	[m]
s_g	Relaxation coefficient	[–]
s_i	Function of the fluid velocity	[–]
$\boldsymbol{S}^g$	Diagonal relaxation matrix in moment space	[–]
t	Time	[s]
$\boldsymbol{u}$	Fluid velocity	[m/s]
V	Volume of liquid	[m^3]
w_i	Weight coefficient	[–]
W	Interfacial thickness	[m]
$\boldsymbol{x}$	Position vector	[m]
β	Parameter related to the chemical potential	[J/m^3]
δ_m	Unit mass	[kg]
δ_t	Time step	[s]
δ_x	Lattice spacing	[m]
θ	Contact angle	[rad]
θ'	Angle described in Figures 7 and 9	[rad]
κ	Parameter related to the chemical potential	[N]
μ	Dynamic viscosity	[Pa s]
μ_ϕ	Chemical potential	[J/m^3]
ν	Kinematic viscosity	[m^2/s]
ξ	Signed distance from the liquid–gas interface	[m]
ρ	Fluid density	[kg/m^3]
σ	Surface tension coefficient	[N/m]
τ_f	Relaxation time for the order parameter	[–]
τ_g	Relaxation time for the fluid velocity	[–]
ϕ	Order parameter	[–]
ψ	Signed distance from the solid–fluid interface	[m]
Ω_i^f	Collision operator for the order parameter	[–]
Ω_i^g	Collision operator for the fluid velocity	[kg/m^3]
Superscripts		
eq	Local equilibrium distribution function	
T	Transpose of a matrix	
$*$	Post-collision and pre-streaming distribution function	
Subscripts		
f	Fluid phase (liquid or gas phase)	
F	Fluid-phase lattice node	
g	Gas phase	
i	Discrete velocity direction	
$\bar{i}$	Opposite discrete velocity direction to i	
l	Liquid phase	
s	Solid phase	
w	Wall surface	

Abbreviations

The following abbreviations are used in this manuscript:

GPU	Graphics Processing Unit
LBE(s)	Lattice Boltzmann Equation(s)
LBM	Lattice Boltzmann Method
MPI	Message Passing Interface
PFLBM	Phase-Field Lattice Boltzmann Method
SRT	Single-Relaxation-Time
WMRT	Weighted Multiple-Relaxation-Time

Appendix A. Implementation of the Conventional Wetting Boundary Condition in Three-Dimensional Systems

This appendix describes the implementation of the wetting boundary condition for three-dimensional systems in which the solid–fluid interface is approximated by a staircase geometry. This implementation extends the wetting boundary condition proposed by Fakhari et al. [29] to three-dimensional configurations. For such staircase-approximated walls, the wall-normal vector at the solid surface is determined using the following procedure, instead of Equation (34).

Step 1. Let "s" denote a solid lattice node adjacent to a fluid lattice node, and let its position vector be $\boldsymbol{x}_\mathrm{s}$. Using the discrete velocity vectors pointing to the six nearest-neighbor lattice nodes of point s, the following vector is computed:

$$\hat{\boldsymbol{n}}^{(\mathrm{sf})} = \sum_i S_i \boldsymbol{e}_i, \tag{A1}$$

where $i \in \{1, \ldots, 6\}$, and S_i is a binary indicator function defined as

$$S_i = \begin{cases} 1, & \text{if } \boldsymbol{x}_\mathrm{s} + \boldsymbol{e}_i \delta_t \text{ is a fluid node,} \\ 0, & \text{if } \boldsymbol{x}_\mathrm{s} + \boldsymbol{e}_i \delta_t \text{ is a solid node.} \end{cases} \tag{A2}$$

If $\hat{\boldsymbol{n}}^{(\mathrm{sf})} \neq \boldsymbol{0}$, the wall-normal vector at point s is obtained as

$$\boldsymbol{n}^{(\mathrm{sf})} = \frac{\hat{\boldsymbol{n}}^{(\mathrm{sf})}}{\left|\hat{\boldsymbol{n}}^{(\mathrm{sf})}\right|}. \tag{A3}$$

If $\hat{\boldsymbol{n}}^{(\mathrm{sf})} = \boldsymbol{0}$, proceed to Step 2.

Step 2. Equation (A1) is evaluated using the discrete velocity vectors pointing to the second-nearest neighbor lattice nodes of point s, where $i \in \{7, \ldots, 18\}$. If $\hat{\boldsymbol{n}}^{(\mathrm{sf})} \neq \boldsymbol{0}$, the wall-normal vector is determined using Equation (A3). Otherwise, proceed to Step 3.

Step 3. Equation (A1) is evaluated using the discrete velocity vectors pointing to the third-nearest neighbor lattice nodes of point s, where $i \in \{19, \ldots, 26\}$. If $\hat{\boldsymbol{n}}^{(\mathrm{sf})} \neq \boldsymbol{0}$, the wall-normal vector is determined using Equation (A3).

Except for highly restricted geometries, such as solid walls with a thickness of only one lattice spacing, the wall-normal vector can be determined by this procedure up to Step 3.

Because the wall-normal vector obtained in this manner is aligned with one of the discrete velocity vectors $\boldsymbol{e}_i$, a fluid lattice node adjacent to point s always exists along the wall-normal direction. Therefore, in this conventional approach, interpolation of the order parameter ϕ_f in Equation (37) is unnecessary. In addition, since the wall position w is located midway between points s and f, the order parameter inside the solid phase ϕ_s is extrapolated by setting $d_\mathrm{s} = d_\mathrm{f} = |\boldsymbol{x}_\mathrm{f} - \boldsymbol{x}_\mathrm{s}|/2$ in Equations (37) and (38).

References

1. Liu, H.; Valocchi, A.J.; Kang, Q.; Werth, C. Pore-Scale Simulations of Gas Displacing Liquid in a Homogeneous Pore Network Using the Lattice Boltzmann Method. *Transp. Porous Media* **2013**, *99*, 555–580. [CrossRef]
2. Liu, H.; Zhang, Y.; Valocchi, A.J. Lattice Boltzmann Simulation of Immiscible Fluid Displacement in Porous Media: Homogeneous versus Heterogeneous Pore Network. *Phys. Fluids* **2015**, *27*, 052103. [CrossRef]
3. Lohse, D. Fundamental Fluid Dynamics Challenges in Inkjet Printing. *Annu. Rev. Fluid Mech.* **2022**, *54*, 349–382. [CrossRef]
4. Xu, R.; Wang, G.; Jiang, P. Spray Cooling on Enhanced Surfaces: A Review of the Progress and Mechanisms. *J. Electron. Packag.* **2022**, *144*, 14–16. [CrossRef]
5. Sugimoto, M.; Miyazaki, T.; Kaneda, M.; Suga, K. Coolant Wetting Simulation on Simplified Stator Coil Model by the Phase-Field Lattice Boltzmann Method. *Entropy* **2022**, *24*, 219. [CrossRef]
6. Swift, M.R.; Orlandini, E.; Osborn, W.R.; Yeomans, J.M. Lattice Boltzmann Simulations of Liquid-Gas and Binary Fluid Systems. *Phys. Rev. E* **1996**, *54*, 5041–5052. [CrossRef]
7. Safari, H.; Rahimian, M.H.; Krafczyk, M. Consistent Simulation of Droplet Evaporation Based on the Phase-Field Multiphase Lattice Boltzmann Method. *Phys. Rev. E* **2014**, *90*, 033305. [CrossRef] [PubMed]
8. Sugimoto, M.; Sawada, Y.; Kaneda, M.; Suga, K. Consistent Evaporation Formulation for the Phase-Field Lattice Boltzmann Method. *Phys. Rev. E* **2021**, *103*, 053307. [CrossRef] [PubMed]
9. Mandegari, A.; Rahimian, M.-H.; Jafari, A.; Jalali, A. Phase-Field LBM Simulation of Evaporation and Condensation in Regular Porous Media: A Unit-Cell Study. *Phys. Fluids* **2025**, *37*, 087161. [CrossRef]
10. Liu, L.; Lee, T. Wall Free Energy Based Polynomial Boundary Conditions for Non-Ideal Gas Lattice Boltzmann Equation. *Int. J. Mod. Phys. C* **2009**, *20*, 1749–1768. [CrossRef]
11. Li, Q.; Luo, K.H.; Kang, Q.J.; He, Y.L.; Chen, Q.; Liu, Q. Lattice Boltzmann Methods for Multiphase Flow and Phase-Change Heat Transfer. *Prog. Energy Combust. Sci.* **2016**, *52*, 62–105. [CrossRef]
12. Ding, H.; Spelt, P.D.M. Wetting Condition in Diffuse Interface Simulations of Contact Line Motion. *Phys. Rev. E* **2007**, *75*, 046708. [CrossRef] [PubMed]
13. Fakhari, A.; Bolster, D. Diffuse Interface Modeling of Three-Phase Contact Line Dynamics on Curved Boundaries: A Lattice Boltzmann Model for Large Density and Viscosity Ratios. *J. Comput. Phys.* **2017**, *334*, 620–638. [CrossRef]
14. Zhang, S.; Tang, J.; Wu, H. Simplified Wetting Boundary Scheme in Phase-Field Lattice Boltzmann Model for Wetting Phenomena on Curved Boundaries. *Phys. Rev. E* **2023**, *108*, 025303. [CrossRef]
15. Jiang, F.; Guo, Y.; Mochizuki, S.; Tsuji, T. Improved Implementation of Wettability in the Phase-Field Lattice Boltzmann Method for Simulating Droplet Impacts on Cylindrical Targets. *Phys. Fluids* **2024**, *36*, 122132. [CrossRef]
16. Huang, J.-J.; Wu, J.; Huang, H. An Alternative Method to Implement Contact Angle Boundary Condition and Its Application in Hybrid Lattice-Boltzmann Finite-Difference Simulations of Two-Phase Flows with Immersed Surfaces. *Eur. Phys. J. E* **2018**, *41*, 17. [CrossRef]
17. Huang, J.-J.; Zhang, L. Simplified Method for Wetting on Curved Boundaries in Conservative Phase-Field Lattice-Boltzmann Simulation of Two-Phase Flows with Large Density Ratios. *Phys. Fluids* **2022**, *34*, 082101. [CrossRef]
18. Chiu, P.-H.; Lin, Y.-T. A Conservative Phase Field Method for Solving Incompressible Two-Phase Flows. *J. Comput. Phys.* **2011**, *230*, 185–204. [CrossRef]
19. Geier, M.; Fakhari, A.; Lee, T. Conservative Phase-Field Lattice Boltzmann Model for Interface Tracking Equation. *Phys. Rev. E* **2015**, *91*, 063309. [CrossRef]
20. Chella, R.; Viñals, J. Mixing of a Two-Phase Fluid by Cavity Flow. *Phys. Rev. E* **1996**, *53*, 3832–3840. [CrossRef]
21. Badalassi, V.E.; Ceniceros, H.D.; Banerjee, S. Computation of Multiphase Systems with Phase Field Models. *J. Comput. Phys.* **2003**, *190*, 371–397. [CrossRef]
22. Liang, H.; Xu, J.; Chen, J.; Wang, H.; Chai, Z.; Shi, B. Phase-Field-Based Lattice Boltzmann Modeling of Large-Density-Ratio Two-Phase Flows. *Phys. Rev. E* **2018**, *97*, 033309. [CrossRef] [PubMed]
23. Bhatnagar, P.L.; Gross, E.P.; Krook, M. A Model for Collision Processes in Gases. I. Small Amplitude Processes in Charged and Neutral One-Component Systems. *Phys. Rev.* **1954**, *94*, 511–525. [CrossRef]
24. Fakhari, A.; Bolster, D.; Luo, L.-S. A Weighted Multiple-Relaxation-Time Lattice Boltzmann Method for Multiphase Flows and Its Application to Partial Coalescence Cascades. *J. Comput. Phys.* **2017**, *341*, 22–43. [CrossRef]
25. Liang, H.; Shi, B.C.; Guo, Z.L.; Chai, Z.H. Phase-Field-Based Multiple-Relaxation-Time Lattice Boltzmann Model for Incompressible Multiphase Flows. *Phys. Rev. E* **2014**, *89*, 053320. [CrossRef]
26. Wang, H.; Yuan, X.; Liang, H.; Chai, Z.; Shi, B. A Brief Review of the Phase-Field-Based Lattice Boltzmann Method for Multiphase Flows. *Capillarity* **2019**, *2*, 33–52. [CrossRef]
27. Bouzidi, M.; Firdaouss, M.; Lallemand, P. Momentum Transfer of a Boltzmann-Lattice Fluid with Boundaries. *Phys. Fluids* **2001**, *13*, 3452–3459. [CrossRef]

28. Yu, Y.; Li, Q.; Wen, Z.X.; Huang, R.Z. Investigation on Boundary Schemes in Lattice Boltzmann Simulations of Boiling Heat Transfer Involving Curved Surfaces. *Phys. Fluids* **2020**, *32*, 063305. [CrossRef]
29. Fakhari, A.; Li, Y.; Bolster, D.; Christensen, K.T. A Phase-Field Lattice Boltzmann Model for Simulating Multiphase Flows in Porous Media: Application and Comparison to Experiments of CO 2 Sequestration at Pore Scale. *Adv. Water Resour.* **2018**, *114*, 119–134. [CrossRef]

Disclaimer/Publisher's Note: The statements, opinions and data contained in all publications are solely those of the individual author(s) and contributor(s) and not of MDPI and/or the editor(s). MDPI and/or the editor(s) disclaim responsibility for any injury to people or property resulting from any ideas, methods, instructions or products referred to in the content.